

Measurement of the $\Lambda_b^0 \rightarrow \Lambda^0 J/\Psi (\rightarrow \mu^+ \mu^-)$
Branching Fraction.

Koen Lambrechts

July 13, 2022

Contents

1	Introduction & approach	3
1.1	A probe for New Physics	3
1.2	Branching fraction	4
1.3	Strategy & Outline	8
2	Theory	9
2.1	Standard Model	9
2.1.1	Leptons	10
2.1.2	Quarks	10
2.1.3	Bosons	10
2.2	Lepton Flavour Universality	12
2.2.1	Tree level and Loop level	13
2.2.2	Experiments	13
2.3	$\Lambda_b^0 \rightarrow \Lambda^0 J/\Psi (\rightarrow \mu\mu)$ decay mode	15
2.3.1	$\Lambda_b^0 \rightarrow \Lambda^0 J/\Psi$	15
2.3.2	$\Lambda^0 \rightarrow \pi^- p^+$	16
2.3.3	The fragmentation fraction $f_{\Lambda_b^0}$	16
3	LHCb	19
3.1	intro - LHC and B factories	19
3.2	LHC	19
3.3	LHCb detector specifics	20
3.4	Tracking system	21
3.4.1	VELO	21
3.4.2	Tracker Turicensis (TT)	22
3.4.3	Magnet	22
3.4.4	Inner and Outer Tracker (T1-T3)	23
3.5	Particle identification system	23
3.5.1	Cherenkov Detector (RICH I & II)	23
3.5.2	Calorimeter (CALO)	24
3.5.3	Muon chambers (M1 - M5)	24
4	Data and Selection	26
4.1	Data samples	26
4.1.1	Collision data	26
4.1.2	Downstream and Longstream tracks	26
4.2	Trigger	26
4.2.1	Level 0 Trigger	29
4.2.2	High Level Trigger 1	29
4.2.3	High Level Trigger 2	30
4.3	Detector Acceptance	30
4.4	Reconstruction	30
4.5	Stripping	30
4.6	PID	33
4.7	Selection	33
4.7.1	Fiducial Cuts	33
4.7.2	Mass cut Λ_b^0/B_d^0	34
4.7.3	Fiducial range of $\frac{f_{L_b}}{f_d}$	34

4.7.4	Simulation Data	35
5	Efficiencies and Weights	36
5.1	Weights	37
5.1.1	Kinematic weights	37
5.1.2	Λ_b lifetime weight	37
5.1.3	Λ_b Angular distribution weight	37
5.1.4	Tracking weights	38
5.1.5	PID stripping weight	38
5.2	Efficiencies	38
5.2.1	Acceptance Efficiency	38
5.2.2	Reconstruction & Selection Efficiency	39
5.3	Efficiency and uncertainty	39
6	Yield	41
6.1	Invariant mass spectrum	41
6.2	Maximum Likelihood Fit	42
6.3	Λ_b^0 Signal shape	42
6.4	B_d^0 Signal shape	43
6.5	Backgrounds	44
6.5.1	Combinatorial Background Shape	45
6.5.2	Peaking Background Shape for Λ_b^0	45
6.5.3	Peaking Background Shape for B_d^0	46
6.6	Total fit shapes	48
6.6.1	Resulting Yield	48
6.6.2	Systematic Uncertainties	48
7	Systematic Uncertainties	53
7.1	Systematic uncertainties of the efficiency	53
7.2	Systematic uncertainties of the fit model	53
8	Results	56
8.1	Efficiency Corrected Yield Ratio	56
9	Discussion	57

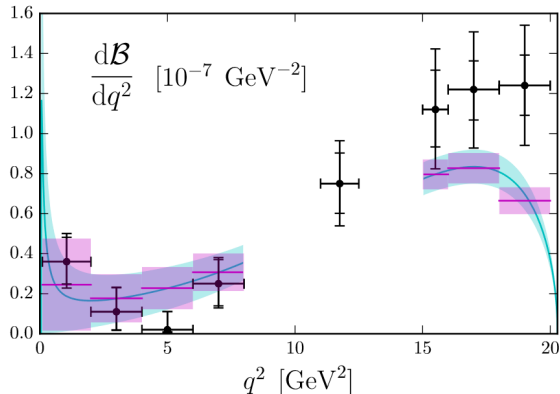


Figure 1: $\Lambda_b^0 \rightarrow \Lambda^0 \mu\mu$ branching fraction as a function of the dimuon invariant mass.

1 Introduction & approach

The unprecedented collision energies that are reached at the Large Hadron Collider (LHC) at CERN, opens up windows for test of theoretical predictions as well as the search for New Physics. A measurement of the branching fraction (BF) of the $\Lambda_b^0 \rightarrow \Lambda^0 J/\Psi$ decay is presented in this thesis. An improved value for this Λ_b^0 decay can be an important step in research on rare decays, as this decay is very useful as a normalization channel in these decays. A good measurement of $\Lambda_b^0 \rightarrow \Lambda^0 J/\Psi$ is required to accurately measure rare decays like $\Lambda_b^0 \rightarrow \Lambda^0 \mu\mu$ at the LHCb. In Figure 1 we can see the branching fraction of this decay as a function of the dimuon invariant mass (q^2) at LHCb with Run 1 data. We note that there is no good measurement or prediction for the window $[7,15] GeV^2$. This is the window where we find the J/Ψ and $\Psi(2s)$ resonance. Furthermore we see two error bars on the data-points, where the outer error is a systematic uncertainty that comes from the known $\Lambda_b^0 \rightarrow \Lambda^0 J/\Psi$ branching fraction. The inner part of the error bar is the statistical uncertainty. The statistical part can be improved by collecting more data, as has been done in Run 2 (and will be done in Run 3) at the LHCb. The systematic contribution of about 25% can only be reduced by an improved measurement of the $\Lambda_b^0 \rightarrow \Lambda^0 J/\Psi$ branching fraction.

1.1 A probe for New Physics

Particle Physics is about discovering the laws and rules that govern all interactions around us. The Standard Model of particle physics (SM) does a very good job in describing most of these interactions. However, we know that the set of rules is not fully complete, as we still lack explanations for some phenomena. Some well known examples of problems not solved by the SM are the matter-antimatter asymmetry of the universe and the existence of dark matter and dark energy.

To incorporate explanations for phenomenons like the matter-antimatter asymmetry, the SM has to be expanded. Since the SM is very well defined

mathematically, adding new theories or expansions of theories will usually entail small alterations in current SM predictions. Therefore, testing SM predictions is a typical approach either to exclude new theories if the prediction is confirmed, or if the prediction is proven wrong get a nod in the right direction to look for new physics. Of course both confirming and discarding a prediction requires very high accuracy and certainty.

A method to test SM predictions is to measure the branching fractions of rare decays. In the LHC proton proton collisions at very high velocity provide enough energy to allow for these rare decays. The LHCb specializes in rare decays involving b-quarks. In order to finish analysis on the full dataset collected by the LHCb, more normalization channels need to be measured. One of these normalization channels is $\Lambda_b^0 \rightarrow \Lambda^0 J/\Psi(\mu^+\mu^-)$, that is for example useful to analyse $\frac{\Lambda_b^0 \rightarrow \Lambda^0 \mu^+ \mu^-}{\Lambda_b^0 \rightarrow \Lambda^0 e^+ e^-}$.

The measurement of this rare decay can in turn be used to use another SM prediction, the concept of Lepton Flavor Universality (LFU). In the theory section we will delve deeper into LFU. Recent analysis of LFU on data collected by the LHCb experiment have drawn a lot of interest.[8] A first analysis was presented, where the result of the the analysis show tension with the SM prediction. In a second analysis of a larger data sample this tension remained. There is thus reason to analyse more data in order to test the LFU predictions.

The relative and absolute branching fraction of $\Lambda_b^0 \rightarrow \Lambda^0 J/\Psi(\mu^+\mu^-)$ will be measured using equation 1, that will be discussed in more detail in the approach section.

1.2 Branching fraction

The *branching fraction* is a term often used in particle physics to describe the frequency with which a certain phenomenon occurs. If we have a branching fraction, e.g. $\frac{\Gamma(K_s^0 \rightarrow \pi^+ \pi^-)}{\Gamma K_s^0}$ of $(69.20 \pm 0.05)\%$, this means that for every thousand times the mother particle (K_s^0) decays, it will decay, on average, 692 times via this decay channel to a $\pi^+ \pi^-$ pair.[30]

As mentioned before, the Standard Model is successful in describing many of the phenomena around us, and we can for one calculate branching fractions. The branching fraction of, for example, $\Lambda_b^0 \rightarrow \Lambda^0 e^\pm \mu^\mp$ is predicted as zero in the SM. However, if we look at models extending the SM, there are models that predict a non-zero Branching fraction for this specific decay. This means that if a decay of $\Lambda_b^0 \rightarrow \Lambda^0 e^\pm \mu^\mp$ would be observed, these New Physics models would become more likely to be true. And if on the other hand, we can put an upper limit on the branching ratio that is significantly smaller than the value predicted by a new model, this would discard this model. Since rare decays have small branching fractions, and are often measured with a relatively large uncertainty, more precise measurements of rare decays are good probe for new physics. Any small discrepancy in a measured branching fraction, if precise enough, can have relatively large implications on standard model predictions.

If we look at the branching fraction of $\Lambda_b^0 \rightarrow \Lambda^0 J/\Psi(\mu^+\mu^-)$ we know that

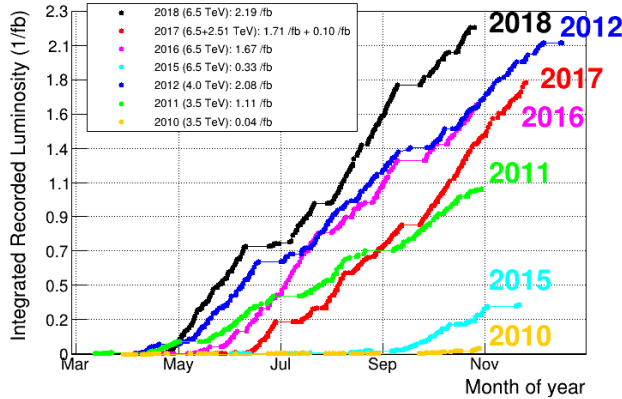


Figure 2: Here we see the integrated luminosity per year in inverse femtobar. The energy per year is the energy per proton, and so the total collision energy is the double of this.

the result in an experiment looks like equation 1:

$$BR(\Lambda_b^0 \rightarrow \Lambda^0 J/\Psi(\mu^+ \mu^-)) = (\mathcal{L}^{LHCb} \cdot \sigma_{pp \rightarrow b\bar{b}} \cdot f_{\Lambda_b^0} \cdot 2)^{-1} \frac{N_{\Lambda_b^0 \rightarrow \Lambda^0 J/\Psi(\mu^+ \mu^-)}}{\epsilon_{\Lambda_b^0 \rightarrow \Lambda^0 J/\Psi(\mu^+ \mu^-)}} \quad (1)$$

Where \mathcal{L}^{LHCb} is the total integrated luminosity of the LHCb detector in $cm^{-2}s^{-1}$, $\sigma_{pp \rightarrow b\bar{b}}$ the $b\bar{b}$ -pair production cross section for the pp-collision, $f_{\Lambda_b^0}$ the hadronization factor (frequency with which the $b\bar{b}$ -pair or b-quark forms a Λ_b^0), $N_{\Lambda_b^0 \rightarrow \Lambda^0 J/\Psi(\mu^+ \mu^-)}$ the number of detected decays (Yield) and $\epsilon_{\Lambda_b^0 \rightarrow \Lambda^0 J/\Psi(\mu^+ \mu^-)}$ the efficiency with which we detect these decays. For clarity we will refer to the $\Lambda_b^0 \rightarrow \Lambda^0 J/\Psi$ Yield and Efficiency from equation 1; as N_{sig} and ϵ_{sig} respectively. The luminosity (\mathcal{L}) per year can be seen in Figure 2.

Equation 1 shows that from the number of observed decays we can determine a branching fraction if we know the value of \mathcal{L}^{LHCb} , $\sigma_{pp \rightarrow b\bar{b}}$, $f_{\Lambda_b^0}$ and ϵ_{sig} well enough. It is often beneficial to introduce a normalization channel, that is similar to the decay and has a well known branching fraction. This way we reduce the relative errors and we can get rid of σ and \mathcal{L} . This leaves us with the Yield (N), Efficiency (ϵ), and hadronization factor $f_{\Lambda_b^0}$ (how often a created b-quark hadronizes into our hadron of interest) for both channels to determine the branching fraction ratio.

There are a few other factors to take into account while deciding on a normalization channel. Preferably the two decays have a similar kinematic and topological structure. These aspects will be discussed shortly with the use of figure 3, 4, and 5. If there are large differences between the signal and normalization decay, differences in detection efficiency throughout the detector come in to play. One of the aspects that can play a role here is (a similar) mass of the mother particle.

Furthermore there should not be too large a difference between the number of events from the signal and normalization channel. If the number of normalization channel decays is much smaller than the signal, the statistical error on the normalization channel will have a significant impact on the error of the ratio.

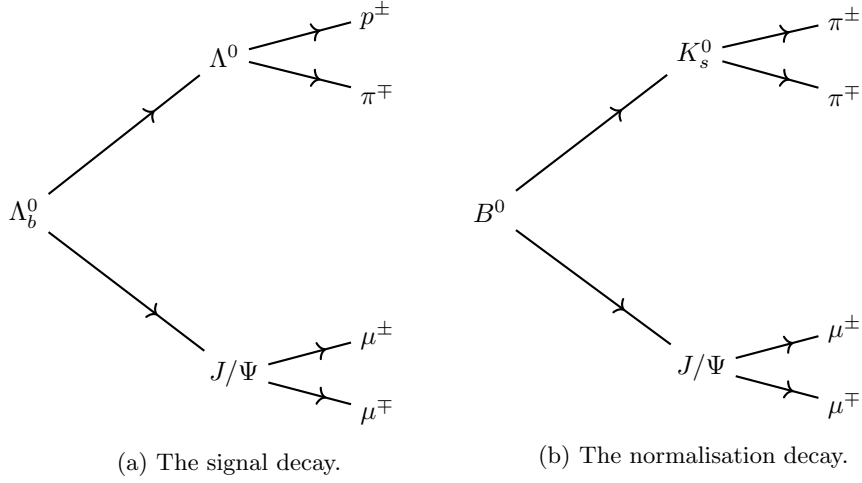


Figure 3: The complete signal and normalization decay

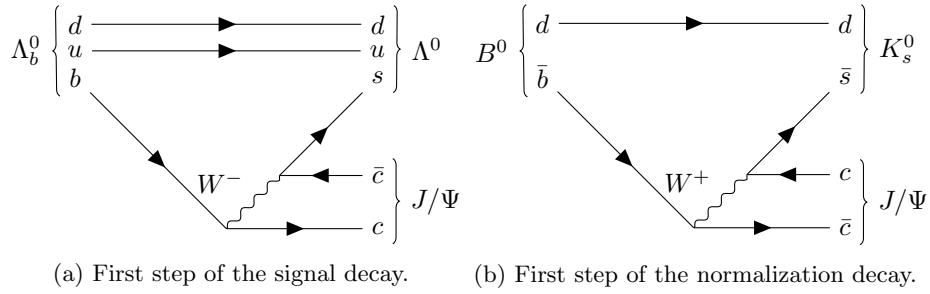


Figure 4: The decay of a Λ_b^0 and B^0 via the signal and normalization channel

With these considerations in mind, we find $B^0 \rightarrow K_s^0 J/\Psi(\mu^+ \mu^-)$ as a suitable normalization channel so that we want to determine the ratio of the branching fractions as in equation 2 where we distinguish between 'sig' and 'norm' channel.

$$\frac{BR(\Lambda_b^0 \rightarrow \Lambda^0 J/\Psi(\mu^+ \mu^-))}{BR(B^0 \rightarrow K_s^0 J/\Psi(\mu^+ \mu^-))} = \frac{(L^{LHCb} \cdot \sigma_{pp \rightarrow b\bar{b}} \cdot f_{\Lambda_b^0} \cdot 2)^{-1} \frac{N_{sig}}{\epsilon_{sig}}}{(L^{LHCb} \cdot \sigma_{pp \rightarrow b\bar{b}} \cdot f_d \cdot 2)^{-1} \frac{N_{norm}}{\epsilon_{norm}}} \quad (2)$$

Or, after dividing out L^{LHCb} and $\sigma_{pp \rightarrow b\bar{b}}$

$$\frac{BR(\Lambda_b^0 \rightarrow \Lambda^0 J/\Psi(\mu^+ \mu^-))}{BR(B^0 \rightarrow K_s^0 J/\Psi(\mu^+ \mu^-))} = \left(\frac{f_{\Lambda_b^0}}{f_d}\right)^{-1} \frac{\frac{N_{sig}}{\epsilon_{sig}}}{\frac{N_{norm}}{\epsilon_{norm}}} \quad (3)$$

Where $\frac{f_{\Lambda_b^0}}{f_d}$ is the ratio between the hadronization factors of Λ_b^0 and B^0 (which is known for LHCb), N_{norm} the number of observed decays for the normalization channel and ϵ_{norm} the efficiency with which we detect the decays from the normalization channel.

The $B^0 \rightarrow K_s^0 J/\Psi(\mu^+ \mu^-)$ decay channel has the same \mathcal{L} and σ , as these are independent of the specific decay. Very useful for this analysis is the fact

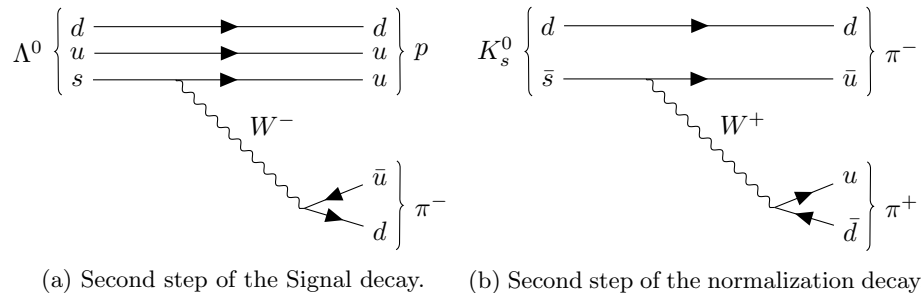


Figure 5: The decay of a Λ^0 and K_s^0 via the signal and normalization channel

that the ratio $\frac{f_{\Lambda_b^0}}{f_d}$ for the LHCb has already been determined in an earlier research by Koopman.[6] The N_{norm} and ϵ_{norm} are simultaneously obtained in a different analysis of the same dataset. If we look at figure 3, 4 and 5 we see that both signal and normalization decay show a similar topology. Both decays have the same number of decay vertices, and two oppositely charged hadrons and two oppositely charged muons in the final state. If we look at the lifetimes of the particles, we notice that $\tau_{\Lambda_b^0}$ ($1.471 \cdot 10^{-12}$) and (τ_{B^0} $1.519 \cdot 10^{-12}$) are very similar. The daughter particles have 1 particle and therefore lifetime in common. We can see that τ_{Λ^0} ($2.632 \cdot 10^{-10}$) and ($\tau_{K_s^0}$ $8.954 \cdot 10^{-11}$) are also of the same order.[1] The decays will transverse the detector in a similar way. With all this we can conclude that we've found a suitable normalization channel to measure a branching fraction ratio.

Determining a branching fraction ratio can be useful by itself. Lepton Flavor Universality tests, which will be discussed in chapter 2, for example make use of ratios between muonic and electronic (semi-)leptonic decays. Determining the absolute branching fraction on top of the ratio, can have some additional benefits and we can in fact do this for our signal channel. The method to do this once again makes use of the favourable choice of our normalization channel. The branching fraction of $B^0 \rightarrow K_s^0 J/\Psi(\mu^+ \mu^-)$ is measured with very high precision in b-factories like Belle II (and before this BaBar).[28] These b-factories are specifically designed to measure decays of B mesons with high precision. The precision of this measurement is much higher than the known value of our ($\Lambda_b^0 \rightarrow \Lambda^0 J/\Psi(\mu^+ \mu^-)$) branching fraction. So if we connect the known absolute branching fraction of the normalization channel to the ratio that we measured with high precision, we can actually extract an absolute branching fraction of our signal channel. As is shown in equations 4 and 5.

$$BR(\Lambda_b^0 \rightarrow \Lambda^0 J/\Psi(\mu^+ \mu^-)) = \alpha \cdot N_{sig} \quad (4)$$

We claim to be able to measure $BR(\Lambda_b^0 \rightarrow \Lambda^0 J/\Psi(\mu^+ \mu^-))$ as given in equation 4. Where α is called the normalization factor that contains everything else present in the ratio as shown in equation 5.

$$\alpha = \frac{BR(B^0 \rightarrow K_s^0 J/\Psi(\mu^+ \mu^-))}{N_{norm}} \cdot \frac{f_d}{f_{\Lambda_b^0}} \cdot \frac{\epsilon_{norm}}{\epsilon_{sig}} \quad (5)$$

As mentioned earlier, to analyse all data collected by LHCb in run 1 and 2, more normalization channels are required. To analyse Λ_b^0 decays, the

$\Lambda_b^0 \rightarrow \Lambda^0 J/\Psi(\mu^+\mu^-)$ decay will in turn be used as a normalization channel. For example to look at $\Lambda_b^0 \rightarrow \Lambda^0 \mu^\pm e^\mp$ or as a normalization channel of the muonic decay $\Lambda_b^0 \rightarrow \Lambda^0 \mu^+\mu^-$. The afore mentioned ratios to test LFU can take the form of equation 6.

$$R_{\Lambda_b^0} = \frac{\Lambda_b^0 \rightarrow \Lambda^0 \mu^+\mu^-}{\Lambda_b^0 \rightarrow \Lambda^0 e^+e^-} \quad (6)$$

Here $R_{\Lambda_b^0}$ is a ratio that can be calculated from the Standard Model. As the ratio given above is still exposed to experimental uncertainties, once again a ratio is introduced. By using separate normalization channels for both the muonic- and electronic-decay we get a double ratio as is shown in equation 7

$$R_{\Lambda_b^0} = \frac{\frac{\Lambda_b^0 \rightarrow \Lambda^0 \mu^+\mu^-}{\Lambda_b^0 \rightarrow \Lambda^0 J/\Psi(\mu^+\mu^-)}}{\frac{\Lambda_b^0 \rightarrow \Lambda^0 e^+e^-}{\Lambda_b^0 \rightarrow \Lambda^0 J/\Psi(e^+e^-)}} \quad (7)$$

In this case various lepton-species related systematic errors drop out. So by introducing a more precisely determined branching fraction of $\Lambda_b^0 \rightarrow \Lambda^0 J/\Psi(\mu^+\mu^-)$ we can measure new ratio's to help test LFU. Analysing these Λ_b^0 decays can be an addition to already published results of LFU-tests[8] Both as means to increase the amount of data, so improved statistics, as well as the introduction of a new and sensitive decay.

1.3 Strategy & Outline

The goal of this research is to find the absolute branching fraction of the $\Lambda_b^0 \rightarrow \Lambda^0 J/\Psi(\mu^+\mu^-)$ decay mode. For this analysis, a total of $5.57 fb^{-1}$ of collision data(CL) collected at the LHCb detector in Run 2 (2016-2018) is used. Furthermore this analysis will only involve DD-track events, which will be discussed in Chapter 4. The LHCb is specialized in decays of mesons and baryons that contain a b-quark. More of the LHCb specifics will be discussed in Chapter 3. Processing selection of the the data is then discussed in Chapter 4. From equation 4 and equation 5 we can see that we need the normalization factor α and the number of detected decays of our signal channel, where α consists of a number of parameters. Two of these parameters, $\frac{f_d}{f_{\Lambda_b^0}}$ [36] and $BR(B_d^0 \rightarrow K_s^0 J/\Psi(\mu^+\mu^-))$ [28][29] are taken from external measurements. Not directly presented in the Equation, but necessary external measurements are these of the well determined branching fraction of $\Lambda^0 \rightarrow p\pi$ and $K_s^0 \rightarrow \pi^+\pi^-$. [29] The two efficiency terms ϵ_{sig} and ϵ_{norm} will be determined and discussed in Chapter 5, whereas the Yield for both N_{sig} and (N_{norm}) which will be discussed in chapter 6. We will discuss the systematic uncertainties due to our method in Chapter 7. With these parameters we can finally present the absolute branching fraction of the $\Lambda_b^0 \rightarrow \Lambda^0 J/\Psi(\mu^+\mu^-)$ decay mode which will be presented in chapter 8. And we will discuss our findings and conclusion in the final chapter 9.

Standard Model of Elementary Particles

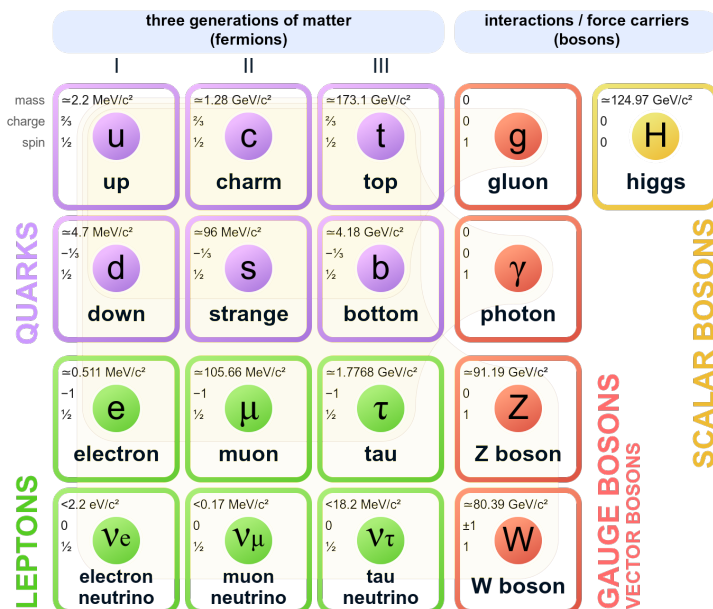


Figure 6: Standard Model of Elementary Particles

2 Theory ¹

In this chapter we will briefly review the SM in general and several aspects that are of particular interest to this research in a little more detail. Finally we'll look at the relevant theory to arrive at our $BR(\Lambda_b^0 \rightarrow \Lambda^0 J/\Psi(\mu^+ \mu^-))$, e.g. $\frac{f_d}{f_{\Lambda_b^0}}$ and $BR(B_d^0 \rightarrow K_s^0 J/\Psi(\mu^+ \mu^-))$ and of course the interactions involved in our signal decay channel.

2.1 Standard Model

Our current understanding of particle physics is captured in the Standard Model. A pictorial version of this very powerful model of the laws governing the physics of elementary particles is shown in figure 6. The SM is a quantum field theory that describes the elementary particles as excitations of their corresponding fields. In figure 6 we see a first distinction between fermions, spin- $\frac{1}{2}$ particles and the spin 1 bosons. Fermions are subsequently split up into leptons and quarks, and within this division into three generations. Together, the fermions make up the elementary building blocks of all matter in our Universe, where as the bosons mediate the interactions between these fermions. Furthermore, for every fermion depicted in figure 6 there's an anti-particle with exactly the opposite charge and quantum numbers.

¹Information presented in this chapter relies heavily on [9], [11] and [10].

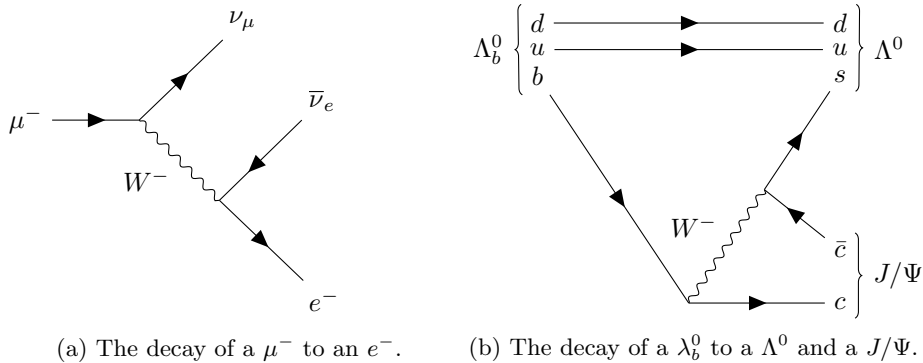


Figure 7: Two different decays involving a W^- boson.

2.1.1 Leptons

The lepton section of the fermions is shown in the bottom-half of figure 6, where we can see the three 'flavours' as e and its ν_e , μ and its ν_μ and τ and its ν_τ . The leptons are observed freely and have an electric charge of ± 1 or 0 . For reactions involving leptons we expect the lepton flavour number to be conserved. This means that for the creation or destruction of each lepton an anti particle of the same flavour should, respectively, be created or destroyed as well. All leptons interact via the weak interaction, the charged leptons also via the Electro Magnetic (EM) interaction and none via the strong interaction.

2.1.2 Quarks

Quarks or anti-quarks have a $\pm \frac{2e}{3}$ or $\mp \frac{1e}{3}$ charge and contrary to leptons, we do not observe free quarks. Instead quarks hadronize into mesons or baryons, to form a particle with 'whole' charge. We call particles that consist of a quark and anti-quark a meson, and a particle that consists of a combination of 3 quarks or anti-quarks a baryon. Also quarks occur in three flavours, as shown in the top-half of figure 6. Quarks interact via all three forces.

2.1.3 Bosons

Besides these elementary building blocks, we have the force mediators in the form of bosons. Most of this analysis deals with the weak force, so we will look into this in some more detail. Besides the weak force we have the strong force that is mediated by the gluon, and the electromagnetic force that has the photon as a force carrier. Both of these bosons are massless and charge-less.

The force most prominently present in this analysis is the weak force, mediated by 3 bosons; the Z^0 , W^+ and W^- boson. The Z^0 boson, that is its own anti-particle, has a mass of about 91 MeV, whereas the W^\pm bosons are somewhat lighter with a mass around 80 MeV. The difference in charge between these three bosons plays a major role in particle decay.

The interaction involving a Z^0 boson is called a *neutral current*, and as far as observed so far neutral currents do not change the flavour or generation of a fermion. For particle decay where we observe a change in flavour or generation, such as is shown in figure 7, we know there is a W^\pm involved. In 3(a) we see

the decay of a μ^- to a ν_μ under emission of a W^- . This W^- in turns decays to an e and an $\bar{\nu}_e$. At both 'ends' of the W^- we have a vertex, and at each vertex we expect conservation of charge and conservation of lepton flavour. So for example in the first vertex we see that charge is conserved by emitting a W^- , while the emitted ν_μ takes care of the flavour conservation.

In figure 7(b) we see a simple hadronic decay where we start out with a b quark (charge $-\frac{1}{3}$) that, under emission of a W^- boson (charge -1), decays to a c quark (charge $\frac{2}{3}$). Here too we see that charge is conserved as we have $-\frac{1}{3} = -1 + \frac{2}{3}$ for the complete vertex. The W^- boson then decays to a \bar{c} and s quark which also conserves charge. In figure 7(b) we do indeed see a flavour or generation change of the quark (from b to c), a process that requires this W^\pm boson or *charged current*. Flavour changing quark interactions do not all have the same likeliness of occurring. The coupling constants of the transitions between quarks are given in the so called Cabibbo-Kobayashi-Maskawa matrix (CKM-matrix) in equation 8:[9]

$$V_{CKM} = \begin{pmatrix} V_{ud} & V_{us} & V_{ub} \\ V_{cd} & V_{cs} & V_{cb} \\ V_{td} & V_{ts} & V_{tb} \end{pmatrix} = \begin{pmatrix} 0.9743 & 0.2253 & 0.0035 \\ 0.2252 & 0.9734 & 0.0412 \\ 0.0087 & 0.0404 & 0.9994 \end{pmatrix} \quad (8)$$

Here $|V_{\alpha\beta}|^2$ gives the transition probability for an $\alpha \rightarrow \beta$ or $\beta \rightarrow \alpha$ transition. What we can see in equation 8 is that the CKM-matrix is highly diagonal, so a transition inside a generation or doublet is preferred. We call such a transition *Cabibbo allowed*, contrary to generation changing *Cabibbo suppressed* interactions. The property of flavour changing quarks comes from the fact that a quark is not in a pure flavour eigenstate, but in fact in a mixture of flavours. This is somewhat similar to the mixing of neutrinos according to the PMNS-matrix. However, the timescale of the mixing differs by many orders of magnitude due to mass differences between leptons and quarks.

The mixture of flavour eigenstates would naively also imply neutral flavour changing transitions e.g. a transition of an s to a d quark. This is however not observed in nature and it is believed that this comes from the cancellation of these processes due to the GIM mechanism. The GIM - mechanism cancels the Strangeness Changing Neutral Current (SCNC) (or, more generally the Flavour Changing Neutral Neutral CUrrent (FCNC)) that pops up in the Cabibbo Matrix. The GIM-mechanism comes from adding the c-quark and making a second doublet. This way the charmed quark was correctly predicted. Adding the expression for the Lagrangian from the Cabibbo theory and the GIM mechanism results in the cancellation of the SCNC-parts. For higher order contributions the same cancellation occurs, although because of mass differences between quarks, there's a little bit of SCNC left. This is in agreement with observations.[9]

Quarks mix and can transit between flavours due to different coupling constants, this is not the case for the lepton part of the fermions. Observations lead physicists to believe that leptons of different flavours all exhibit the same coupling constants. There could however still be some kind of difference, that has yet to be found.

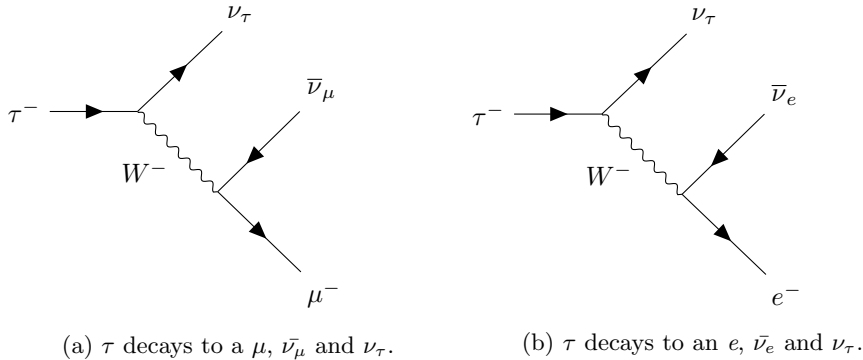


Figure 8: The leptonic decay of a τ . For both decays lepton numbers are preserved.

2.2 Lepton Flavour Universality

The Standard Model is a crucial but incomplete description of the fundamental particles and interactions in physics. One of the aspects that has recently drawn interest is that of Lepton Flavour Universality (LFU). The SM assumes lepton universality, meaning that the coupling constants for all three lepton flavours are identical. LFU has been tested and confirmed in experiments at *tree level* [1], but with the ongoing developments in experimental physics possibilities have opened up to test LFU at higher order decays.

We should note that the mass of all three neutrinos ν_e, ν_μ, ν_τ is much smaller than that of all other particles. Furthermore $m_e \ll m_\mu \ll m_\tau$ and $m_{e,\mu,\tau} \ll m_{W,Z}$.

Lepton Universality assumes that *'the interaction of the e and its ν_e are identical with those of the μ and its associated ν_μ and the τ and its ν_τ , provided the mass differences are taken into account.'*[10] This statement is in fact an assumption, as no fundamental reasoning enforces this behaviour. It is however in agreement with all experimental data.

We will briefly look at some examples of lepton decays to illustrate this universality. Since the mass difference between different lepton flavours is so large, we can ignore the mass of the leptons in the final state. The reasoning behind neglecting the mass of leptons in the final state is based on phase space arguments. In simple words, the rest masses of the leptons in the final state are very small compared to the total momentum, so that there's enough 'room' for infinite combinations of momenta of the products in the final state, regardless of the exact mass of the lepton.

We will first consider the decay rate of a muon to an electron shown in figure 7(a), which involves the rate (Γ), the Fermi coupling constant (G_F) that mediates the interactions, the muon mass (m_μ) and some dimensionless constant K . Dimensional analysis tells us that, with Γ dimension [E], G_F dimension [E]⁻² and m_μ dimension [E] we expect an expression of the rate of the form

$$\Gamma(\mu^- \rightarrow e^- + \bar{\nu}_e + \nu_\mu) = K G_F^2 m_\mu^5, \quad (9)$$

LFU implies that if we replace the μ and ν_μ on the left by a τ and ν_τ respectively, on the right hand only the mass changes to m_τ , while K remains

basically the same. In this case we are looking at the τ decay shown in figure 8 on the right. If the τ were to decay to a μ we would have the situation shown on the left in figure 8. We can see that both decays depend on the same weak force carrier, the W^- boson, and have two interaction vertices (one upon creation of the boson and one upon decay of the boson) and are very similar as a whole. Considering this τ -decay, we expect from $e - \mu$ universality that equation 10 holds.

$$\Gamma(\tau^- \rightarrow e^- + \bar{\nu}_e + \nu_\tau) = \Gamma(\tau^- \rightarrow \mu^- + \bar{\nu}_\mu + \nu_\tau). \quad (10)$$

Or in other words, we expect the τ to decay as often to an electron as a muon. This is in agreement with the measured branching fractions of 0.178 and 0.174 for the electron and muon mode respectively, which are equal within error.[31] We have seen the basics of LFU and the fact that it upholds in a basic example, but we will now move on to new experimental options to test LFU in higher orders.

2.2.1 Tree level and Loop level

A decay can take place via different decay modes. A decay mode where only a single interaction with a force carrier (boson) is involved is often called a tree level decay. Such a decay is shown on the left in figure 9. The point where the three lines come together is the interaction *vertex* of the boson with the fermions. Tree decays make up the majority of the decays. Decays can however look much more complicated, and these type of decays are collectively called loop level decays. The basic rule is that a loop decay has two extra vertices, and of course, the more loops you get, the more vertexes you get. A simple version of such a loop level decay is shown on the right in figure 9. So in principle more than one loop can be involved. However in general with the increase in loops, the occurrence of the decay decreases.

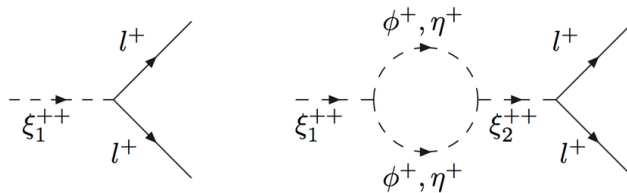


Figure 9: We see a generalized form of a decay, where the left figure depicts a Tree level and the right figure depicts a Loop level.[12]

Loop level decays can give rise to more exotic physics, but are more difficult to do research on. Contributions from loops are generally suppressed, leading to small perturbations of the tree-level results, or rare decay. As a consequence high experimental sensitivity is needed.

2.2.2 Experiments

The LFU tests performed on tree level decays have confirmed the assumption of LFU. Recently new experiments, testing LFU for loop level decays have been

performed. For example, at the Large Hadron Collider. With the number of events that the LHC is able to produce at the high energy of $\sqrt{13}$ TeV, we are now able to get a big enough data sample to get statistics on rare (loop level) decays to test LFU. Several different experiments are performed, of which 2 types are most important for our LFU case. One type are experiments involving loop level b-quark decay of the form

$$b \rightarrow s l^- l^+ \quad (11)$$

where we have a so called leptonic decay of a particle to another particle via the process of a bottom-quark (b) decaying to a strange-quark (s), while emitting a lepton anti-lepton pair ($l^- l^+$). This is a flavour-changing neutral current, and thus not tree-level.

A second type of experiment looks at semileptonic beauty decays of the form

$$b \rightarrow c l^- \bar{\nu}_l \quad (12)$$

where this time the beauty-quark decays to a charmed-quark (c). Furthermore a lepton and an anti-lepton neutrino are created to preserve charge and lepton number have been performed.² This is a SM allowed decay via the charged current.

Data has been collected for both types of experiments, and the combination of results of those experiments that have already been fully analysed do in fact show tension with LFU.[8] We will describe the experiments searching for $b \rightarrow s l^- l^+$ by means of an introduction.

Currently $b \rightarrow s l^- l^+$ with electrons and muons in the final state are accessible, meaning that we can collect enough data on these decays to get a meaningful result.[8] The goal of these experiments is to determine the ratio given in equation 13:

$$R_H = \frac{BR(B \rightarrow H \mu^+ \mu^-)}{BR(B \rightarrow H e^+ e^-)} \quad (13)$$

where H stands for a hadron and R_H is the ratio of the branching fraction of the muon decay mode to this hadron 'H' over the branching fraction of the electron decay mode.

To account for the detector efficiency in both muon and electron detection, a normalization channel is introduced

$$R_H = \frac{\frac{BR(B \rightarrow H \mu^+ \mu^-)}{BR(B \rightarrow H J/\Psi(\rightarrow \mu^+ \mu^-))}}{\frac{BR(B \rightarrow H e^+ e^-)}{BR(B \rightarrow H J/\Psi(\rightarrow e^+ e^-))}} \quad (14)$$

Here the branching fraction for both electron and muon decay mode of $B \rightarrow H J/\Psi(\rightarrow l^+ l^-)$ is well known in theory and confirmed match experiments. As mentioned earlier, the inclusion of this extra ratio effectively cancels the detector specific effects.

One of the tested decay channels was $B^+ \rightarrow K^+ l^+ l^-$, resulting in a ratio of



$$R_K = 0.745_{-0.074}^{+0.090}(stat) \pm 0.036(syst), \quad (15)$$

²The final state of a leptonic decay contains a lepton anti-lepton pair, where as a semileptonic decay has a lepton and its corresponding neutrino in the final state.



which is in tension with the standard model prediction of 1.0 with a significance of 2.6σ . [13]

As Lepton Flavor Universality is supposed 'up to a correction for mass,' not all ratios are expected to be the same. Combining them into one ratio is thus difficult, however the results of all fully analysed experiments have been combined to a result that is in tension with the SM prediction with a significance of (Should still fill this in) .

2.3 $\Lambda_b^0 \rightarrow \Lambda^0 J/\Psi (\rightarrow \mu\mu)$ decay mode

- Here the cross section comes in $\sigma_{pp \rightarrow b\bar{b}}$ 
- With some luminosity L 

$$p^+ p^+ \xrightarrow{\text{L}} b\bar{b} \xrightarrow{\sigma_{pp \rightarrow b\bar{b}}} \Lambda_b^0 \xrightarrow{f_{\Lambda_b^0}} \Lambda^0 J/\Psi \rightarrow \mu^- \mu^+ \pi^- p^+ \quad (16)$$

- Here the hadronization factor comes in $f_{\Lambda_b^0}$ 
- Here the branching fraction comes in $BR(\Lambda_b^0 \rightarrow \Lambda^0 J/\Psi)$ 

An improved measurement of the $\Lambda_b^0 \rightarrow \Lambda^0 J/\Psi (\rightarrow \mu\mu)$ branching fraction can be of use to improve the LFU tests, so we should now turn to the theory of the specifics of this analysis. We can look at the schematic given in equation 16 to see the different steps in this full process of creation, decay and detection of our analysis. In yellow and blue we see that the we should get information on the the luminosity at the point of the pp-collision and information on the cross section from how many $b\bar{b}$ -pairs are created. As mentioned before, getting exact information on this is very difficult, which is why we use a normalization channel to get rid of these terms.

In red we have the hadronization factor $f_{\Lambda_b^0}$ that plays a role when the b quarks hadronize. This term will be discussed in a bit, but we'll start with the part in green. The decay of the Λ_b^0 . The Λ_b^0 can decay via many modes, but we are specifically interested in modes where we end up with a Λ^0 and J/Ψ .

2.3.1 $\Lambda_b^0 \rightarrow \Lambda^0 J/\Psi$

We have seen that a decay can occur via tree or loop level decays. The dominant mode for $\Lambda_b^0 \rightarrow \Lambda^0 J/\Psi$ decay is the tree level. In figure 10 we see the tree decay mode of our decay. We have two spectator quarks in the form of a down (d) and an up (u) quark, that do not undergo any transition on their way to arrive in the Λ^0 state. The third quark present in the Λ_b^0 is the beauty (b) quark and in fact the one that decays. In this mode it does so by emitting a W^- boson while decaying to a charmed (c) quark. With the quark generations and the CKM-matrix in mind, we can see that this decay is Cabibbo suppressed, as the $b \rightarrow c$ transition does not conserve generation. The emitted W^- boson decays to a strange (s) and anti-charmed (\bar{c}), where the s joins the two spectator quarks to form the Λ^0 while the $c\bar{c}$ -pair together forms the J/Ψ .

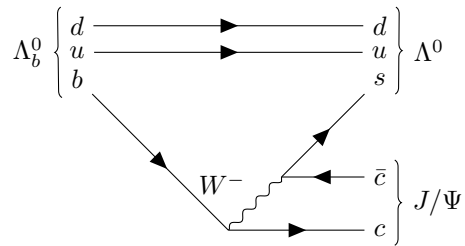


Figure 10: The tree decay mode of $\Lambda_b^0 \rightarrow \Lambda^0 J/\Psi$.

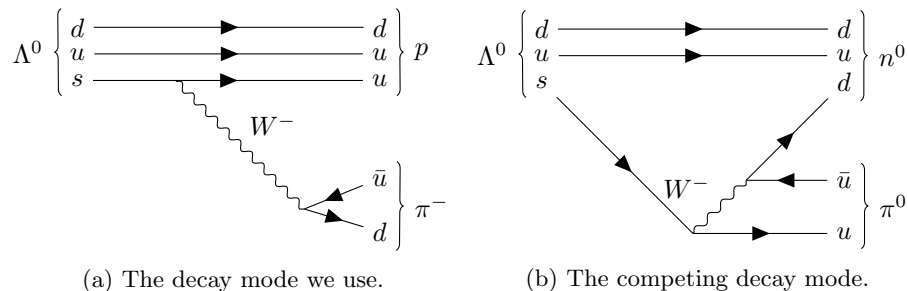


Figure 11: The tree decay modes for hadronic Λ^0 decay.

2.3.2 $\Lambda^0 \rightarrow \pi^- p^+$

Just like for our mother particle, the tree mode decay for the $\Lambda^0 \rightarrow \pi^- p^+$ is the dominant mode. There are in fact two dominant tree decay modes with different final state particles, namely $p^+ \pi^-$ and $n^0 \pi^0$. In figure 11 we see the two most common (hadronic) decay modes for the Λ^0 . Although we can detect neutral particles with the LHCb, detecting charged particles can give much better momentum resolution and thereby decrease the error on our measurement. This is both a reason to look for daughter particles of the Λ^0 and to pick the decay mode shown in figure 11(a) to detect the Λ^0 . In this figure we again see the same spectator d and u quarks. The s quark emits a W^- boson, while transitioning into an u quark that forms the proton. The boson decays into a down and anti-up quark to form the π^- .

2.3.3 The fragmentation fraction $f_{\Lambda_b^0}$.

If we know what the decay modes of $\Lambda_b^0 \rightarrow \Lambda^0 J/\Psi$ look like and we know how to detect them, the only requirement left to find the branching fraction is how many Λ_b^0 there were in the first place. As we can see from equation 16, we need the luminosity (L), the cross section $\sigma_{pp \rightarrow b\bar{b}}$ and the hadronization factor or fragmentation fraction $f_{\Lambda_b^0}$. We already discussed that the Luminosity and production cross section are taken care of by using a normalization channel. This is also useful for $f_{\Lambda_b^0}$.

The fragmentation factor tells us how many b quarks hadronize to a certain beauty hadron. We know that b quarks dominantly hadronize into a meson, as the baryons make up a total of about 9 percent of all hadrons formed by b quarks. Most prominent are the f_u and f_d , which are taken to be equal as their

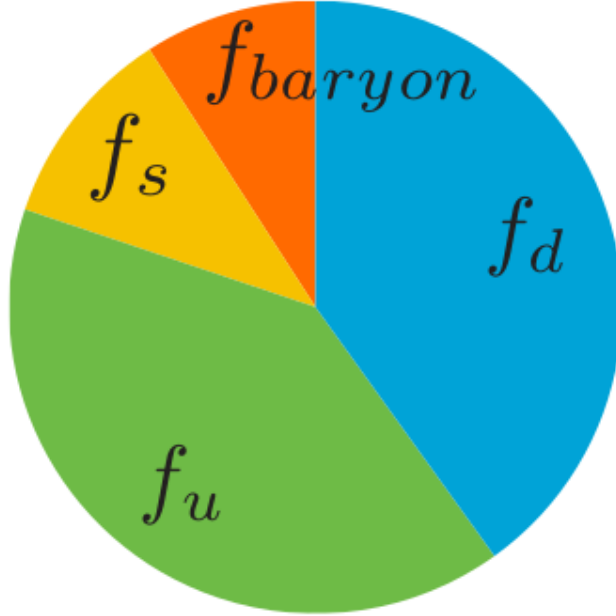


Figure 12: The relative sizes of the hadronization factor of the b-quark.[4]

difference in mass plays no role at these energy scales, followed by f_s . The f_c is almost not existing. Of course we have that:

$$f_u + f_d + f_s + f_c + f_{baryon} = 1. \quad (17)$$

Of this 9 percent of beauty baryons, the dominant hadronization channel is $f_{\Lambda_b^0}$, which makes sense if we consider the quark content. Apart from the b quark, the Λ_b^0 consists of the two lightest quarks u and d. This baryon will therefore be easiest to form.

Measuring these relative production rates of beauty hadrons is not as straightforward as it might seem at first. Apart from regular challenges, these fragmentation fractions also depend on the kinematics of the $b\bar{b}$ -pair. This means that the $f_{\Lambda_b^0}$ can and will depend on P_T and η . Furthermore, determining the absolute value of $f_{\Lambda_b^0}$ runs in to the same type of problems as for the branching

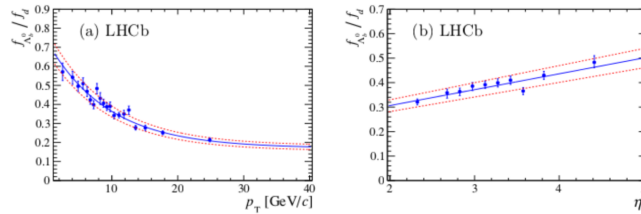


Figure 13: Graph taken from Koopman(2015), where the p_T and η dependence of the hadronization ratio is shown. Meant as an indication, not exact analysis.[6]

fractions. Therefore also here, a ratio instead of absolute value is often used. The latest LHCb $\frac{f_{\Lambda_b^0}}{f_d}$ has been determined by Koopmans (2015) as can be seen in (nog figuur). Here f_d is the hadronization factor of the B^0 meson that serves as our normalization channel. What can be seen in figure 13 is the P_T and η dependence of this ratio. An efficiency corrected average of $\frac{f_{\Lambda_b^0}}{f_d}$ can be determined and will most likely give us a good enough result for our branching fraction of $\Lambda_b^0 \rightarrow \Lambda^0 J/\Psi (\rightarrow \mu\mu)$. To account for the P_T and η dependence, our analysis will only make use of events where the P_T of the mother particle falls within the range [4000,25000] MeV and the η falls within the range [2,5].

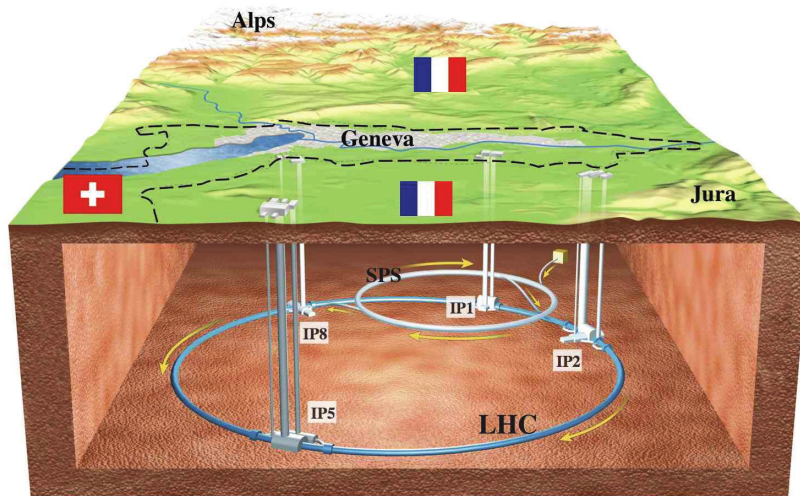


Figure 14: Geographical picture of the LHC site.

3 LHCb³

3.1 intro - LHC and B factories

With the theoretical knowledge in hand we can now move on to how to actually detect the decay of $\Lambda_b^0 \rightarrow \Lambda^0 J/\Psi (\rightarrow \mu^+ \mu^-)$ at LHCb. Research builds on earlier achievements, and for this measurement specifically the efforts of Babar and Belle-II must be acknowledged.[28] At these so called b-factories experiments are performed, specifically dedicated to production and detection of decay of beauty hadrons. These measurements allow us to use the very precise value of the branching fraction of our normalization channel ($B^0 \rightarrow K_s^0 J/\Psi (\rightarrow \mu^- \mu^+)$) as a checkpoint for the determination of our branching fraction. For the rest this research depends on results produced by the LHCb collaboration and the performance of the LHCb detector.

3.2 LHC

In figure 14 we see the scale and location of the Large Hadron Collider (LHC) underneath the Geneva Lake. The LHC is part of CERN and replaced the older Large Electron-Positron collider (LEP) to reach higher collision energy. The core of this huge experimental set up is the tunnel build for its predecessor with a circumference of 26.7 kilometre. Connected to this tunnel are the LINAC2, PSB, PS and SPS to get the particle acceleration started, as well as the 4 main detectors, as is shown in figure 15.

In the LHC two beams of protons (p^+) are collided at the 4 points where the detectors; ATLAS, ALICE, CMS and LHCb are placed. Before entering the main LHC, the protons are already accelerated, however most of the acceleration to reach the energies of 7 TeV happens in the main LHC. This accelerating start at the linear accelerator LINAC2, after which the protons run trough three

³Information presented in this chapter relies heavily on [4], [7] and [2].

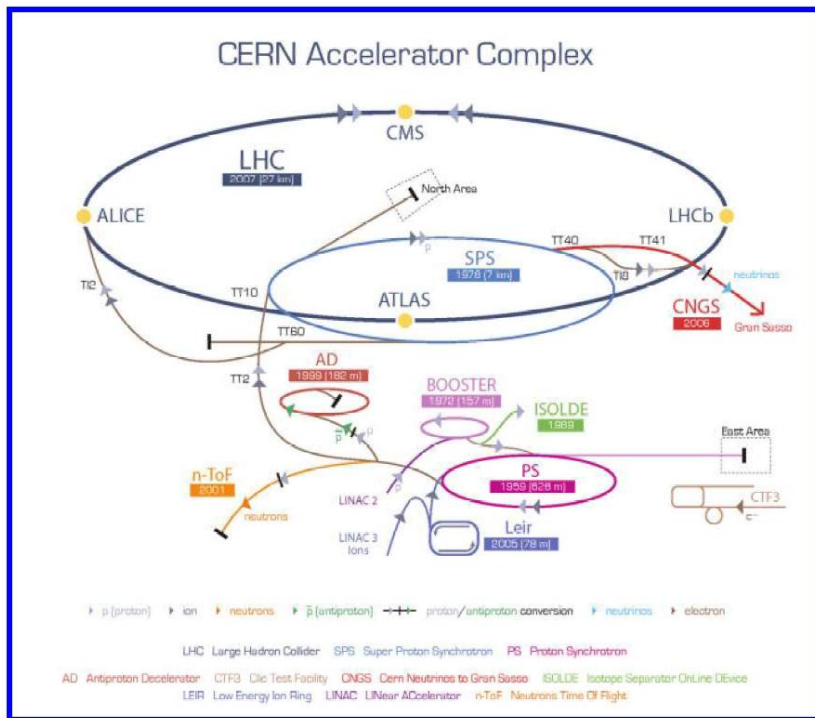


Figure 15: Schematic overview of the different components and detectors of the LHC accelerator complex.

circular accelerators, PSB, PS and SPS before being injected into the LHC. The LHC was built to reach higher collision energy than its predecessor, but of course this didn't come for free. One example of the new difficulties is the fact that two positively charged particles are collided, whereas the LEP used two oppositely charged particles. This means that the LHC must make use of two different magnetic fields to guide the particles in opposite direction through the tunnel. For our research we make use of data from the LHCb detector, which will be discussed next in some detail.

3.3 LHCb detector specifics

In figure 16 a schematic drawing of the LHCb detector is shown. Note that the detector has a specific design connected to its orientation. It is a spectrometer focused on a forward direction. Where detectors like CMS are often designed as a cylinder, to cover a wide angle around the collision point, LHCb is designed in a cone-like shape, to cover a relatively small angle around the forward direction of the beam. The LHCb project opted for this design as its primary objective is to detect (the decay of) b-mesons created in the pp-collisions. The $b\bar{b}$ quarks pairs that form in pp-collisions have a preferred momentum along the beamline. Consequently the beauty hadrons formed from these b quarks will be concentrated in the forward direction along the beam line.

The LHCb is thus specifically designed for b-meson events, which resulted in

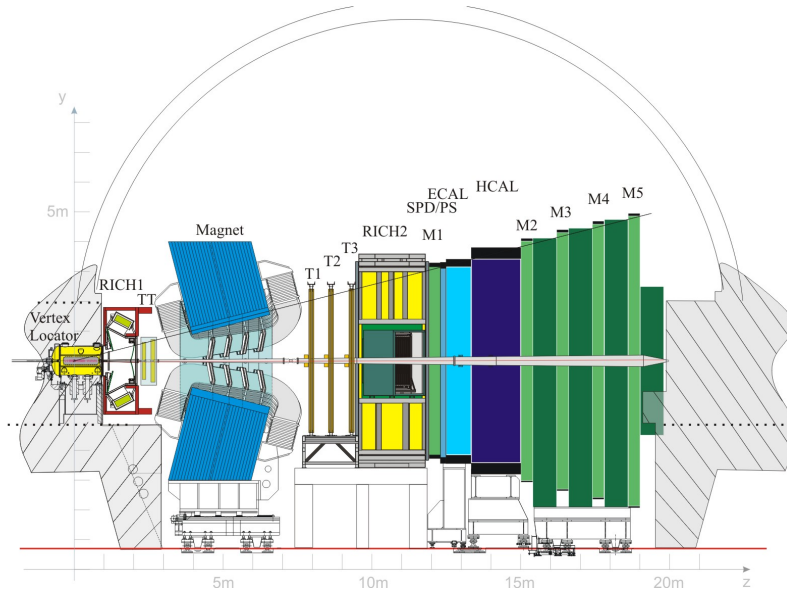


Figure 16: A top view intersection of the LHCb detector.

a design that covers tracking of particles in a range from 10 to 300 mrad in the horizontal plane and 10 to 250 mrad in the vertical plane. A more commonly used parameter is the *pseudo-rapidity* η given in equation 18.

$$\eta \equiv -\ln\left(\tan\frac{\theta}{2}\right) \quad (18)$$

Here θ is the polar angle, which is 0 along the beam line (z-axis). The LHCb covers the pseudo rapidity region: $1.9 < \eta < 4.9$. Figure 17 shows the angular distribution of the $b\bar{b}$ -pairs and the acceptance of the detector.

The full detector is 20 meters long and 5 meters high and wide, making space for a collection of subdetectors, all dedicated to specific parts of the measurement of particles and their decays. We will go over the tasks of these subdetectors in the order that a particle traversing the whole detector would encounter them.

3.4 Tracking system

The subdetectors can be roughly divided into two systems, namely the *tracking system* and the *particle identification system*. First up is the tracking system as this system is located closest to the pp-interaction point. Its goal is to reconstruct the tracks and vertices of the (charged) particles.

3.4.1 VELO

The VELO (short for VERTex LOcator) is a detector that is located directly at the interaction point. The detector is constructed from a series of 21 silicon strip detectors with a thickness of $300 \mu\text{m}$. These detectors are equipped with a ϕ and R sensor and produce a signal ('hit') when a charged particle passes. The goal of

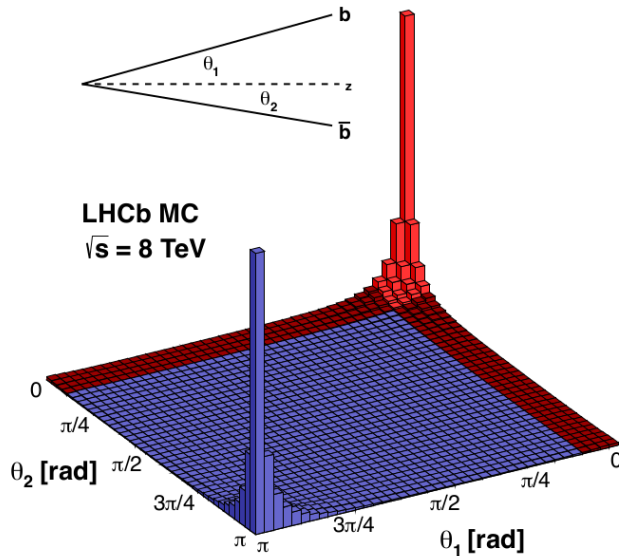


Figure 17: Angular distribution, with respect to the proton-beam, of the produced $b\bar{b}$ -pairs, with the LHCb detector acceptance shown in red.[4]

the VELO is twofold. First to reconstruct the point of the first interaction, the so called *primary vertex*. Second is to locate the *secondary vertex*, which is the point where the formed beauty hadron decays. The primary vertex can usually be located from the abundance of tracks that are produced by the collision. There are always a lot of charged particles created here. The secondary vertex can be identified from charged particles produced in the b-hadron decay. If however there are no charged particles produced, as in the decay mode we are looking at, the reconstruction of the secondary vertex comes from information of other subdetectors. In analysis decays that have hits inside the VELO and behind the magnet are dubbed 'LongLong' (LL), whereas decays that have only charged particles that are picked up behind the VELO are called 'DownDown' (DD).

3.4.2 Tracker Turicensis (TT)

Closely behind the VELO comes the Tracker Turicensis, that is likewise build from semi-conducting silicon strips. The TT serves as a tracker to improve the resolution from the tracks already picked up in the VELO. Furthermore it can also pick up tracks of longer lived neutral particles, that decay outside the VELO e.g. the K_s^0 and our Λ^0 .

3.4.3 Magnet

Following the TT, we find a magnet that serves as a tool to measure the momentum of particles. For this momentum measurement it is beneficial to pick up the charged particle in front of the magnet, to find a track without influence

from the magnetic field as well as the effected track. These particles will in principle have a measured momentum with a higher resolution.

3.4.4 Inner and Outer Tracker (T1-T3)

Downstream the magnet the particles encounter the Inner (IT) and Outer Tracker (OT), that consist of three tracking stations (T1 - T3) that are like so indicated in figure 16. The IT is located closely around the z-axis and is much like the TT. Its goal is to pick up the magnetically bend track of charged particles that have hits in the TT (and VELO) and to track charged particles that decay only behind the magnet. For the analysis of the $\Lambda_b^0 \rightarrow \Lambda^0 J/\Psi$ decay we will see that this latter role is quite important, as the Λ^0 lives rather long.

The OT is part of the same three tracking stations, but located further away from the beam- or z-axis and much larger than the TT. The silicon strips that are used for the VELO, TT and IT are rather expensive, and to save on expenses the OT consists of gaseous straw-tubes. These gas detectors also produce an ionization current, but have a lower resolution than the silicon strips. This lower resolution is a downside, but it is partly compensated by the fact that the detector lies further away from the z-axis. This gives particles that are tracked here a larger angle towards the z-axis and therefore a larger distance to the pp-collision point, which will still result in a high accuracy measurement of the track. Of course, the OT being the largest of the tracking detectors means that the cost saving on material is most efficient here.

3.5 Particle identification system

For a full reconstruction of the decay chain, the tracks need to be assigned a particle identity. This is the purpose of the Particle identification system that is mainly located downstream the tracking system.

3.5.1 Cherenkov Detector (RICH I & II)

Section one of this particle identification system are two Ring Imaging Cherenkov detectors (RICH I & II). The first of which is located right behind the VELO. This RICH I is tasked with measuring low momentum (up to 60 GeV) particles. The RICH II is downstream from the final tracking stations.

Particles moving through a medium with a velocity greater than the local speed of light ($\frac{c}{n}$) will radiate. This radiation is analogous to the emission of a sonic boom, and is called Cherenkov radiation. The Cherenkov radiation is emitted as a cone of light where the opening angle θ of this cone is given by

$$\cos(\theta) = \frac{1}{n\beta}. \quad (19)$$

Here n is the index of refraction of the medium and $\beta = \frac{v}{c}$ with v the speed of the particle, and c the speed of light. The RICH detectors measure the θ and together with information from other sub detectors the mass of a particle can be determined. The Cherenkov detectors can help distinguish between muons, pions, kaons and protons.

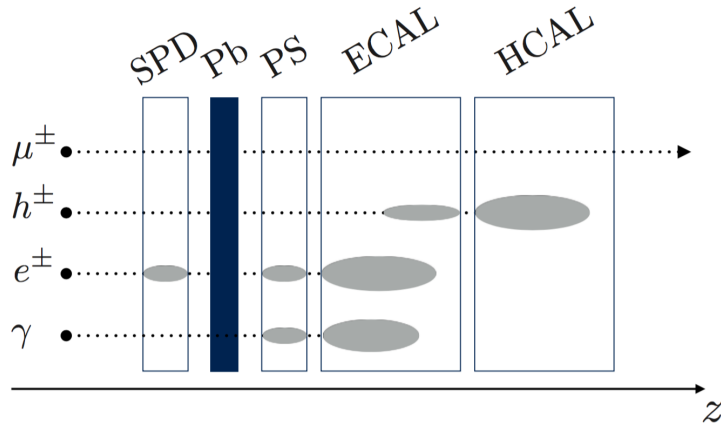


Figure 18: Energy deposit

3.5.2 Calorimeter (CALO)

The CALO is designed in such a way that particles traversing the CALO collide with the material to produce an electromagnetic or hadronic particle shower. The CALO consists of different parts, pointed out in figures 16 & 18, that can together detect these different types of showers. We can see from figure 18 the difference in energy deposit between different types of showers and the different tasks of the CALO system. The Scintillator Pad Detector (SPD) measures the occupancy of events, which can be used by the trigger to decide not to store an event if the occupancy is too high. The Pb is a piece of lead, placed to keep as many disturbing particles out as possible. The Pre-Shower (PS) registers the origin of a shower.

Then follow the two main calorimeters, first the Electromagnetic Calorimeter (ECAL) followed by the Hadronic Calorimeter (HCAL). We can see that photons will mostly deposit energy in the PS and the ECAL. Electron induced showers will likely start already before the Pb, but have their main deposit in the ECAL. The hadrons reaching the calorimeters will induce showers with some energy deposit in the ECAL, but the largest deposit will be in the HCAL. The spatial distribution of the energy deposit in the transverse direction can be used to determine the transverse momentum (P_T) of the particles.

Due to the loss of intensity of the showers, the exact structure and build of the different parts of the CALO is rather complex. A nice and concise explanation is given by Tolk.

3.5.3 Muon chambers (M1 - M5)

Due to their nature, muons will not interact in the CALO, but reach all the way to the muon chambers. The LHCb has a total of five muon chambers, of which M1 is located upstream and M2 - M5 downstream the CALO. The muon detectors 2 - 5 function on the premise that any particle reaching these chambers must be a muon. For a decay with muons in the final state, like the one focused on in this analysis, the muon chambers are essential in the first trigger decision.

For a more elaborate explanation of the working of the muon system we refer to Kuindersma 2018.[2]

4 Data and Selection

The LHCb detector collects the data, which undergoes multiple processing steps before it is suited for data analysis. In this chapter we will first look at these steps before going into the different data samples we use.

4.1 Data samples

In this thesis we discuss the data that is collected from 2016-2018. There are difference between the samples, that we will shortly discuss here. First of all we have 'real' data, or *collision data* and simulated data or *Monte Carlo data*. We will go into these two types of data in some more detail below. Next we have to take into account with what exact settings and tuning we are collecting the data. There is for example the Magnet Up or Magnet Down state of the magnet in the detector. This should not make a large difference for our research, but we still have to look at the samples separately, otherwise difference caused by the polarisation of the magnet can go unnoticed. Finally there can be differences between the exact settings of the detector during a run. One method to account for this is by weighing over the Luminosity of a year. For smaller changes we can apply weights, as we will see in the determination of the trigger efficiency.

4.1.1 Collision data

The Collision data is the data collected by the detector that we have to find our signal decay in. The data collected for these runs is given in Luminosity in. table 1. The storage of the Ntuples is done by year. And for each year the efficiency and number of decays is determined and weighted over the \mathcal{L} .

4.1.2 Downstream and Longstream tracks

We have two different track types in our data, called 'Downstream-tracks' and 'Longstream-tracks.' As we can see in figure 20 the L-tracks have information from the VELO, where as the D-tracks lack this information. Logically the two final state hadron tracks that reconstruct our Λ^0 or K^0 must both be of the same type, to form a DD- or LL-event. For our research we are only interested in DD-events, as analysis of the LL-events has already been done.

4.2 Trigger

In order to analyse the events that are produced at the LHC, we first need to store these events. The vast amount of collisions means not every signal can be stored. The job of the trigger is to decide whether or not to store an event. In figure 21 we can see that the number of registered collisions is immense. The trigger is designed to process around 40 MHz of these collisions, where each

	2016	2017	2018
\sqrt{s} (TeV)	6.5	6.5	6.5
\mathcal{L} (fb ⁻¹)	1.67	1.71	2.19

Table 1: Luminosity and centre of mass energy per proton per year.

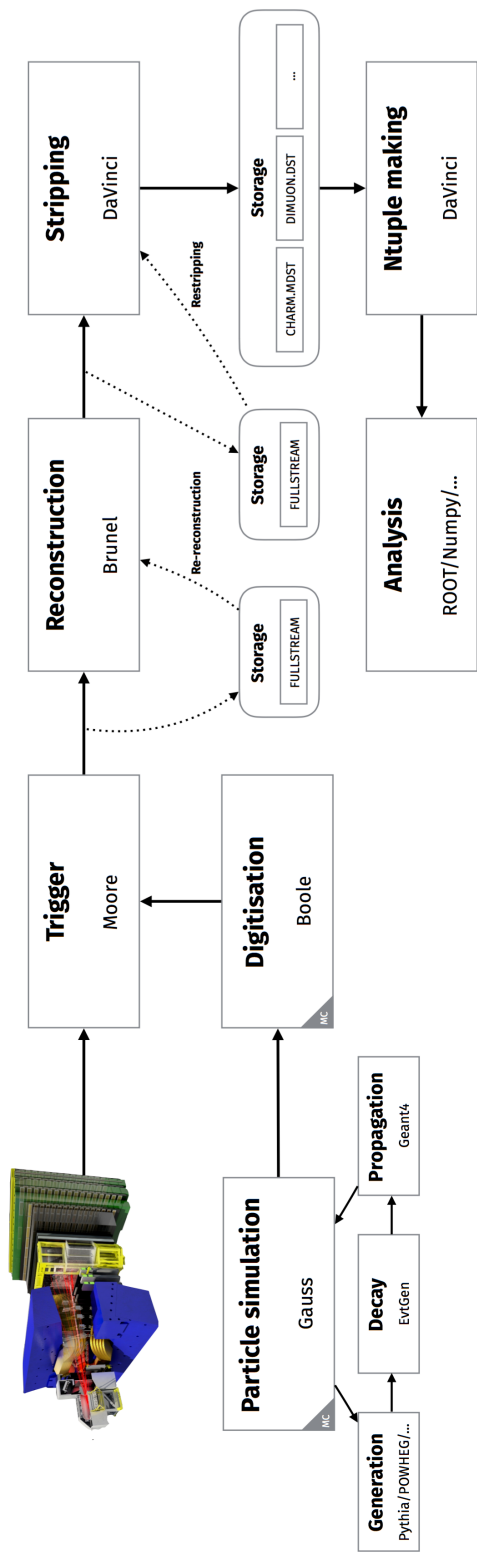


Figure 19: The LHCb data-flow and the software used at different stages.

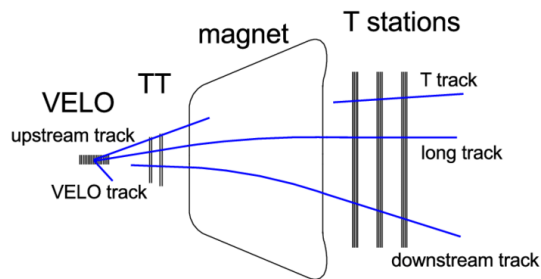


Figure 20: Creative Commons Attribution 3.0 Unported

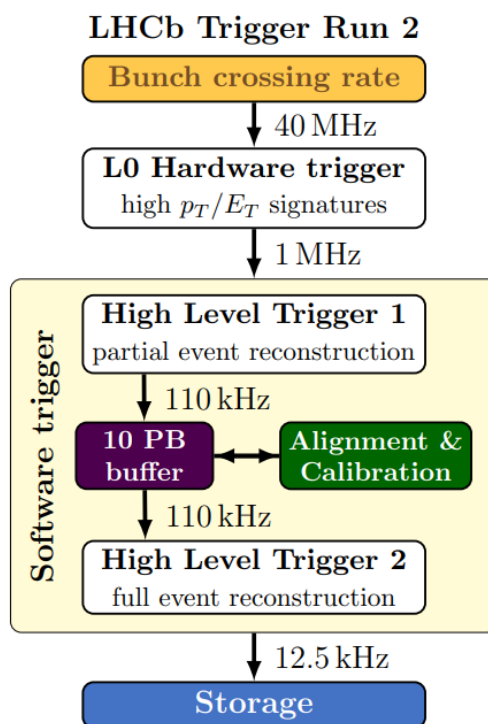


Figure 21: Different steps for the LHCb trigger.

collision event is a collection of hits that surmounts to about 100 kilo bytes. Saving all these events would ask for an incredible bandwidth so the trigger aims for a reduction of the rate to about 12.5kHz. This still requires a bandwidth of about 500 Mbytes/s. In order to improve the likelihood of reconstructing b-hadron decays, the trigger is divided into three stages. The first part is the hardware trigger called L0. The second and third step are independent software triggers, called High Level Trigger 1 and 2 (or HLT1 and HLT2). Each trigger runs over the event that have past the previous stage. The full data-flow of the LHCb, starting at the trigger, is shown in figure 19. We will now look in a bit more detail at these Triggersteps.

4.2.1 Level 0 Trigger

The L0 is a hardware trigger that is built to take a total of $4\mu s$ to make a decision whether to move the event on to the next phase of the trigger or to throw it away. As this requires speed, the L0 only uses information from the fastest subdetectors, the calorimeters (HCAL and ECAL) and the muon chambers. This means that the L0 does not look at the full event information, this only happens in the next stages. The L0 itself consists of three trigger parts, the L0-Muon, L0-Calorimeter and L0-PileUp. The first two look for events that contain two tracks per quadrant of the muon detector that point to a vertex in or around the interaction (collision) region. For these tracks the P_T is determined, as we require some P_T to allow for a good analysis. In case of the muon detectors, the resolution of this P_T is around 20%. If we find a muon, electron or hadron with enough P_T or E_T or, for two muons, a large enough $P_T * P_T$ we get a positive trigger decision. The L0-PileUp looks at something completely different. It looks at information from the SPD part of the CALO to determine the luminosity of the event. If the luminosity is too high, analysing this event would be very time inefficient and so it can veto this event. An event has to pass both the P_T and SPD requirement to pass the L0 trigger.[25] This results in an output rate for the L0 of approximately 1 MHz.

4.2.2 High Level Trigger 1

The HLT1 performs a track-based reconstruction, for which it uses software called *Moore*. [25] The HLT1 uses the information from the VELO detector to reconstruct a Primary Vertex (PV) with at least 5 tracks originating from it in a region of $300\mu m$ around the PV^{mean} . Specifically designed trigger lines with thresholds and constraints on for example number of OT and IT hits, track momentum (p) or impact parameter (IP/χ^2) are applied. There are about 38 trigger lines for the HLT1.

We only use events triggered by muon(*L0Muon*) or dimuon(*L0Dimuon*) lines, of which *L0Muon* is the most prominent. For these events the reconstruction process can be sped up. The reconstruction software uses the information from the VELO to identify a window in the M3 muon chamber wherein it searches for hits. From the information from the VELO and M3, it can reconstruct a track and look for more hits in the other chambers to confirm the track and improve the resolution. The most important decision taken for our data set in the HLT1 is whether or not we have a particle with enough hits and a enough P_T , or a particle that passes the muon PID requirement. This results

in an output of around 80 kHz as can be seen in figure 21.

4.2.3 High Level Trigger 2

The HLT2 is capable of fully reconstructing the events using the same software as the offline reconstruction in run 1. Trigger lines in HLT2 can be divided into two categories, *exclusive* and *inclusive* lines. Exclusive trigger lines target specific final states and require a full reconstruction of all decay particles and tracks in the final state. For our data, most important are the inclusive lines. Inclusive lines can trigger on the decay of a b-hadron with two charged particles in the final state. The most important lines for our data are $J/\Psi(\rightarrow \mu\mu)$ lines and topological lines, where we trigger on a 2 or 3 body decay. We can once again look at figure 21 to see that the output of the HLT2 has a rate of about 5 kHz, which results in about 500 MB/s. These events are then stored in their entirety with the additional information of how they are triggered, so the rest of the analysis can be done offline.

4.3 Detector Acceptance

As mentioned in chapter 3 the LHCb is a forward detector. This means that not all simulated particles fall in the spatial range of the detector, and we need to determine the Acceptance Efficiency. We know that both the signal and normalization decay have two muons in the final state. Therefore we apply a cut on the pseudorapidity (η), the direction of a particle relative to the beam axis. More specifically we do a cut on the two muon candidates for the final state where the η of both muons has to fall within [1.596,5.298].

4.4 Reconstruction

In Run 1, the next step was to run the fully optimized reconstruction offline. In run 2, this is strictly speaking not any longer necessary as the full reconstruction is also run in the Trigger. However, we still use the offline reconstruction for this research, as a sort of insurance that everything runs as it should. For the reconstruction we make use of *Moore* from the HLT as well as *Brunel*. All particle tracks are fully reconstructed and the particle properties like momentum and PID are determined. In order for an event to pass the reconstruction phase, it must at least have four final state particles that are not consistent with the primary vertex. Furthermore, the muon tracks must have a large enough chance that the particle is really a muon, given as a low *GhostProb*. In principle we would also apply this requirement to the two hadrons, but since we are only looking at DD-tracks this is not possible, so for the hadrons we just check if the hadrons are indeed from a DD-track. Finally we require the hits to be consistent with the track. The fully reconstructed event is then passed on to the stripping phase.

4.5 Stripping

In the stripping phase we apply selections to reconstructed properties. In general most requirements in the stripping are relatively loose and aimed to remove background. When there are more strict requirements we try to apply these to

well defined parameters like the PT. The stripping line we use is Bu2LLK_mm, and is designed for decays of the forms given in equations 20, 21 and 22.

$$B^+ \rightarrow K^+ \mu^+ \mu^-, \quad (20)$$

$$B_d^0 \rightarrow K_s^0 \mu^+ \mu^-, \quad (21)$$

$$\Lambda_b^0 \rightarrow \Lambda^0 \mu^+ \mu^- \quad (22)$$

As there are no requirements on the invariant mass of the muon pair, decays with a an intermediate J/Ψ (or $\Psi(2S)$) resonance are also selected by this stripping line. We can see the full set of requirements for this stripping line in table 2.

The muons must fulfill both the isMuon and hasMuon requirement, meaning that the candidates have hits in the muon subsystem and these combined hits are consistent with a muon. Also the muon must have enough transverse momentum and at least somewhat of an impact parameter χ_{IP}^2 . A non zero impact parameter means that the track does not point directly to the primary vertex. meaning that it comes from an intermediate particle.

For the J/Ψ we have no lower bound, and a loose upper bound for the mass window. We then have a somewhat narrower constraint on the χ_{vtx}^2 for the tracks of the muon candidates. Furthermore we have a χ_{FD}^2 constraint with respect to the flight distance of the J/Ψ from the PV. Lastly the χ_{IP}^2 and PT must have a positive value.

The pions and protons only have to pass two requirements to pass the stripping. We need enough momentum on all particles to successfully reconstruct the tracks of the hadrons to build the full decay tree. Finally we need the particles to have at least some χ_{IP}^2 with respect to the PV.

The requirements for the neutral strange hadron are threefold. A minimum PT is requested. Secondly we set a wide mass window. This mass window seems tighter than the previous two, but effectively it is still wide since we see almost all signal candidates within a much narrower range. A last requirement is set for the χ_{vtx}^2 where the tracks of the two charged hadrons must together form a consistent vertex.

For the mother particle (Λ_b/B_d^0), we see a wide mass window for the reconstructed mass, because we want to keep events in a large invariant mass spectrum. Furthermore, we see an upper bound on the χ_{vtx}^2 which assures that the best tracks for the daughter particles form a consistent vertex. The χ_{FD}^2 requirement makes certain the particle is separated from the primary vertex. The χ_{IP}^2 requires an impact parameter that is not too large, meaning that the (Λ_b/B_d^0) is consistent with production from its primary vertex. Finally a DIRA requirement is set, which is a cosine function of the angle between the reconstructed track from the Primary to Secondary vertex and the reconstructed momentum of the (Λ_b/B_d^0). If the full momentum is reconstructed this angle should be close to 0, and the DIRA should be close to 1.

After the stripping phase we can follow up with more selections for the specific decay we are interested in.

Λ_b/B_d^0	
$\ m - m_{\text{PDG}}\ $	$< 1500 \text{ MeV}/c^2$
χ_{vtx}^2	< 27
χ_{FD}^2	> 100
χ_{IP}^2	< 25
DIRA	> 0.9995
J/Ψ	
m	$< 5500 \text{ MeV}/c^2$
χ_{vtx}^2	< 9
χ_{FD}^2	> 16
χ_{IP}^2	> 0
p_T	$> 0 \text{ MeV}/c$
μ^\pm	
isMuon	TRUE
hasMuon	TRUE
p_T	$> 350 \text{ MeV}/c$
χ_{IP}^2	> 9
Λ^0/K_S^0	
p_T	$> 400 \text{ MeV}/c$
$\ m - m_{\text{PDG}}\ $	$< 64 \text{ MeV}/c^2$
χ_{vtx}^2	< 25
p, π	
p	$> 2 \text{ GeV}/c$
χ_{IP}^2	> 4

Table 2: Overview of the Bu2LLK_{mm} stripping line requirements.

4.6 PID

We have an isMuon parameter for all events, that is binary. For simulations the outcomes of this binary decision differ slightly from the data. We determine the efficiency of a muon candidate passing the isMuon requirement that is a function of the kinematic properties of the muon by making use of a data calibration sample. Instead of an explicit PID cut, we apply this weight as a PID cut on the MC when we determine the efficiency. We will come back to this weight in chapter 5.

4.7 Selection

In the selection phase we apply tighter selection rules to filter the data for our specific decay. We have heavy mother particles so we do not need to worry too much about peaking background. Furthermore we do not have to deal with missing particles, as we reconstruct all our final state particles. With the selection cuts we aim to make the signal peak in our invariant mass spectrum (the invariant mass spectrum will be discussed in more detail in Chapter 6) stand out better. This means that we will apply cuts in the phase space of the parameters where the ratio between signal and background events, $\frac{S}{B}$ gives us a high rejection of background and a low loss of signal. We will use the invariant mass spectrum to separate signal from background.

Many cuts or selection rules can be applied without too much thought, as they have no or almost no signal loss. This automatically means that there is a very high background to signal rejection ratio, which is in general the goal of most cuts. The background to signal rejection ratio is described in equation 23.

$$R = \frac{S}{S + B}, \quad (23)$$

Where we have R as the rejection rate, B the number of background events rejected and S the number of signal events rejected. The sum of S and B thus make up the total number of rejected events.

In general it's good to have a high rejection rate, there are however two 'conditions' to keep in mind. We want to optimize our cut point so that we get the smallest possible uncertainty, meaning that we need to keep enough signal events. Furthermore, we do need to keep enough background, to accurately model and fit the background portions of the invariant mass spectrum.

We can see the selection cuts in table 3 and 4. They vary slightly, but they are more or less the same for both Signal channel and Normalization channel. As mentioned in chapter 1 we only look at DD tracks.

4.7.1 Fiducial Cuts

We apply a set of fiducial cuts on the daughter particles Λ^0 (or K_s^0) and J/Ψ . Here we make sure that the Λ^0 (or K_s^0) has at least some lifetime, but not so much that it would have flown out of the detector. We also require that the track of the Λ^0 (or K_s^0) is not consistent with the primary vertex (χ_{FD}^2). Furthermore, we require that the Λ^0 (or K_s^0) has not traversed the detector too far [ENDVERTEX_Z], as this would make it more likely that this is a random particle, not connected to the PV.

Λ_b	
η	[2,5]
PT	[4000,25000] MeV
DTF_L0_JPs_PV_M[0]	[5300,6100] MeV/c ²
DTF_L0_JPs_PV_status[0]	=0
J/Ψ	
$\ M - 3096.916\ $	< 50 MeV/c ²
Λ^0	
ENDVERTEX_Z	[0,2250]
$\ M - 1115.68\ $	< 10 MeV/c ²
χ_{FD}^2	> 0
DIRA_OWNPV	> 0
$\tau*1000$	[0.5,2000] μs

Table 3: Overview of the Λ_b^0 selection cuts.

To assure that we filter out tracks that are reconstructed as one of the daughter particles, but are misidentified, we apply a mass cut on both. The reconstructed mass of the Λ^0 or K_s^0 must be without 10 and 15 MeV respectively of the PDG mass of the particle. This cut seems strict at first, when we compare it to the other cuts in the table. However, the Mass peaks of both the L^0 and the K_s^0 in the reconstructed mass spectrum are rather narrow, which means that there is still not much loss of signal due to this cut. As a check, we did a study to test if the mass window on the daughter particles could be set even smaller than this. The result was that this would still give a very good rejection ratio. However, we decided to keep the boundaries as they were set originally. For the J/Ψ we require the reconstructed mass to be within 50 MeV window of the PDG.

4.7.2 Mass cut Λ_b^0/B_d^0

For the mass of the mother particle we set the mass cut a little different. Here we reconstruct the mass of the mother particle from the 4 momenta of the daughter particles, where we force the daughter particles tracks to the primary vertex. A so called J/Ψ and $\Lambda^0 K_s^0$ constrained. We also require the Decay Tree Fitter to have successfully applied this constrains. These requirements minimize the width of the peak of the signal in the invariant mass spectrum. The mass cut itself is optimized to get rid of peaking backgrounds that we can completely remove, while keeping enough information on the background that we have to incorporate in our fit model. This results in a rather wide mass window. The masswindows we apply are [5150, 6150] for the Λ_b and [5180, 5600] for the B_d^0 .

4.7.3 Fiducial range of $\frac{f_{L_b}}{f_d}$

We have mentioned in chapter 1, that we use a previously determined value for $\frac{f_{L_b}}{f_d}$. This production fraction is well determined within a range of PT and η , so we have to apply a cut on these values for the mother particles. The PT of the mother particles must be in the [4000, 25000] MeV Window, and the pseudorapidity (η) must be within [2,5].

B_d^0	
η	[2,5]
PT	[4000,25000] MeV
DTF_K0_JPs_PV_M[0]	[5300,6100] MeV/c ²
DTF_K0_JPs_PV_status[0]	=0
J/Ψ	
$\ M - 3096.916\ $	< 50 MeV/c ²
K^0	
ENDVERTEX_Z	[0,2250]
$\ M - 497.61\ $	< 15 MeV/c ²
χ_{FD}^2	> 0
DIRA_OWNPV	> 0
$\tau*1000$	[0.5,2000] μs

Table 4: Overview of the B_d^0 selection cuts.

4.7.4 Simulation Data

Monte Carlo (MC) data is simulated data, that mimics a real pp collision as closely as possible. In this analysis, simulation is used to determine the efficiency of the trigger, reconstruction and stripping and selection requirements for signal in data samples. Furthermore it is used to determine invariant mass shapes of signal and background after all requirements have been applied.

MC data is produced centrally at CERN and the route the data takes is shown schematically in Figure 19. The simulated data enters the processing procedure of collision data at the High Level Trigger. The simulation samples that can be processed by the HLT are generated with the LHCb simulation software Gauss. The GAUSS software package contains amongst other packages the ones used to generate our events:PYTHIA, EvtGen and GEANT4.

PYTHIA generates the pp collision(s) which results in a set of true particles produced in this pp collision(s). We are only interested in primary events where a $b\bar{b}$ -pair is created, that hadronizes into a Λ_b^0 or a B_d^0 . EvtGen then simulates the decay process. Once again we have a preferred decay, in our case that is either the signal or normalization channel. Separate datasets are produced for signal and normalization, but in both cases one of the b-quarks is forced to decay via the exact decay channel we want. The propagation through the detector, interaction with the detector and further decay of particles is then simulated by GEANT4. The detector response, the first step in the signal processing, is simulated by the software package BOOLE. Finally, a version of Moore prepares the simulated events which can then be treated the same as real data. Compared to collision samples, the MC samples have some extra information, most importantly the tracks can be matched to a true particle that was generated and has propagated through the detector. In this research we use simulated samples of the generation and decay of the b-hadrons, and of the progression of the decay through the detector. For the generation samples the conditions are the same for all years, so we only need a Magnet up and Magnet Down sample for both b-hadrons. For the other simulation we use different samples per b-hadron, polarization and year. [17][16][4]

5 Efficiencies and Weights

To find the total number of $\Lambda_b^0 \rightarrow \Lambda^0 J/\Psi(\mu^+\mu^-)$ decays that occurs in the LHCb detector, we must understand how efficient our detection process is. We achieve this by determining the efficiency of each reconstruction and selection requirement used in this analysis. Since we are determining a ratio of two branching fractions, we in fact want to determine the efficiency ratio that we see in equation 3, meaning that we will have to determine the reconstruction and selection efficiency for both the Signal and Normalization decay. Making the measurement less sensitive to mismodelling, especially with respect to muons. We use Monte Carlo simulated data to determine these efficiencies. The simulation performs very well overall but is not perfect in certain aspects. We apply weights as a correction for these imperfections. These weights are discussed in the weights section. Lastly we should note that we apply a fiducial cut on the B_d^0 and Λ_b in order to be able to use the LHCb production ratio $\frac{\sigma_{\Lambda_b}}{\sigma_{B_d^0}}$ that has been measured but is only reliable in the specific PT and η region given in table 3. We apply this cut first to all Monte Carlo or Collision samples we use, so that we do not have to take this in to account in the efficiency.

$$\frac{\epsilon_N}{\epsilon_S} = \frac{\epsilon^{Acc,N} \cdot \epsilon^{Trig,N} \cdot \epsilon^{Rec,N} \cdot \epsilon^{Strip,N} \cdot \epsilon^{PID,N} \cdot \epsilon^{Sel,N}}{\epsilon^{Acc,S} \cdot \epsilon^{Trig,S} \cdot \epsilon^{Rec,S} \cdot \epsilon^{Strip,S} \cdot \epsilon^{PID,S} \cdot \epsilon^{Sel,S}} \quad (24)$$

In Equation 24 we see the full efficiency ratio where S stands for Signal and N stands for Normalization. We can see that the full efficiency consists of the Acceptance (Acc), Trigger ($Trig$), Reconstruction (Rec), Stripping ($Strip$), Particle Identification (PID) and Selection (Sel) efficiencies. These parts will be discussed in their dedicated sections.

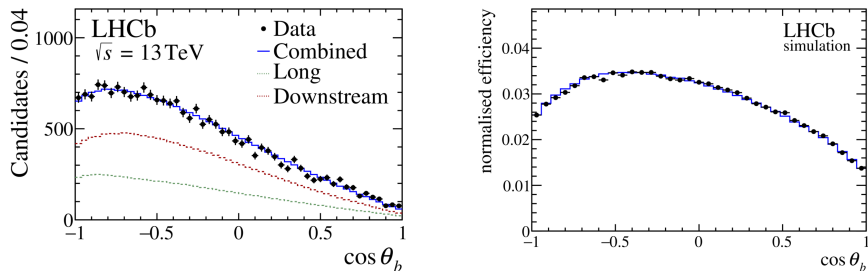


Figure 22: Λ_b candidates in 2016 data (left) and detection efficiency in 2016 MC (left) as a function of the decay angle of the Λ ($\cos(\theta_b)$).

5.1 Weights

As mentioned before, the efficiency ratio is determined on simulated data. While the simulation is a good approximation of the actual data, there are some discrepancies. We can correct for a discrepancy by applying a *per-event weight*. By applying a weight, the over- or underestimation of the Monte Carlo efficiency can be corrected. This results in a systematic uncertainty, that we will discuss in chapter 7. We use a total of five weights, where the Kinematic weight and the Λ_b^0 weights are applied at all stages of the analysis, while the Tracking and PID stripping weights enter the analysis in the Reconstruction stage.

5.1.1 Kinematic weights

The parent particles (Λ_b and B_d^0) are simulated through the simulation of a collision of two protons, where a $b\bar{b}$ -pair is created and one of these quarks hadronizes into a (Λ_b/B_d^0). From comparison between data and simulation, we see that there is a discrepancy between the kinematic properties of the simulation and data. Therefore we apply a weight for both decay channels to correct for this mismodelling in the simulation.

5.1.2 Λ_b lifetime weight

The simulation software used to make our MC samples had the Λ_b -lifetime as an input parameter. However, there has since then been an improved measurement of the lifetime. We apply an analytical weight to correct for this difference. Since this weight is concerned with a Λ_b property only, we apply this weight only to the Λ_b -decay.

5.1.3 Λ_b Angular distribution weight

There is another weight that applies only to the Λ_b -decay. There is a difference between the simulation and data concerning the angular distribution of the daughter particles of the Λ_b . The simulation uses a phase space model, that has significant effects in Λ -decay.[34] In Figure 22 we see a discrepancy between data on the left and MC on the right. The physics that results in an asymmetry in the decay of the Λ is not taken into account which gives rise to this discrepancy.

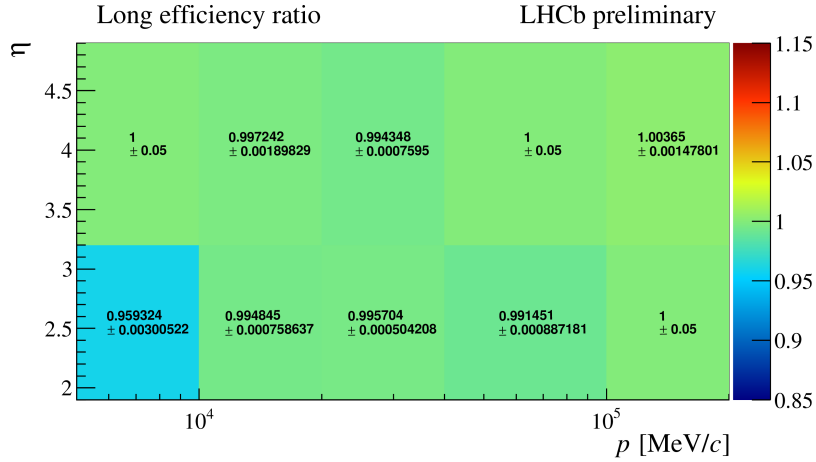


Figure 23: We see the tracking efficiency as a function of p and η

5.1.4 Tracking weights

If we look at Figure 23 we can see a discrepancy distribution of the efficiency in MC that is dependent on η and the PT of the track.[35] To correct for this we add a set of weights, for all final state particles. We apply this weight for both Normalization and Signal channel.

5.1.5 PID stripping weight

The last weight could also be seen as a PID cut on the sample, as we have mentioned in chapter 4. If we apply the isMuon efficiency for both muon candidates in an event and multiply these efficiencies we get the PID stripping weight, which is a direct efficiency. This weight typically ranges from [0.9,1] and has a mean of approximately 0.95.

5.2 Efficiencies

We have seen in equation 24 that the total efficiency consists of many terms, which we will discuss in short below. Eventually we can easily combine most terms so that we end up with two terms, given in equation 25 where only the *Acceptance* term is still determined separate from the rest, as the method is slightly different. All other terms are combined in the *Reconstruction&Selection* term, which is calculated in one go.

$$\frac{\epsilon_N}{\epsilon_S} = \frac{\epsilon^{Acceptance,N} \cdot \epsilon^{Reconstruction\&Selection,N}}{\epsilon^{Acceptance,S} \cdot \epsilon^{Reconstruction\&Selection,S}} \quad (25)$$

5.2.1 Acceptance Efficiency

The Acceptance Efficiency is determined in the same way for both decay channels. The η distribution of the muons is determined by the distribution of the generated b-hadrons. Information of the distribution comes from the simulation of pp collision, where we force the creation of (at least) one $b\bar{b}$ -pair. Furthermore

we force one of these b-quarks to decay via our chosen decay channel, the other b-quark follows any physically allowed decay channel. This simulation only depends on the collision conditions, and these are the same for all years in run 2 of the LHCb. Therefore, we do not need a separate value for the Acceptance Efficiency for each year. We do however need a value for both magnet Up and Down states for both decay channels. To account for discrepancies between MC- and Collision-data we apply the Kinematic and (for the Λ_b^0) the Angular and Lifetime weights. The resulting Acceptance efficiencies are shown in Table 5.

	Λ_b	B_d^0	$\frac{B_d^0}{\Lambda_b}$
18_MD	0.7759 ± 0.0006	0.8029 ± 0.0006	$1.0349 \pm 0.0012\%$
18_MU	0.7759 ± 0.0006	0.8028 ± 0.0006	$1.0347 \pm 0.0012\%$

Table 5: The weighted ϵ^{Acc} for Λ_b and B_d^0 per year and polarization as well as the efficiency ratio.

5.2.2 Reconstruction & Selection Efficiency

The *Reconstruction & Selection Efficiency* is the combined efficiency of the Trigger, Stripping, Reconstruction and Selection Phase. All weights described in the previous section are applied to determine this efficiency. Since there are differences between years, we must determine an efficiency for all years and polarizations. The resulting efficiencies and efficiency ratio are shown in Table 6.

	Λ_b	B_d^0	$\frac{B_d^0}{\Lambda_b}$
16_MD	0.02035 ± 0.00017	0.03796 ± 0.00009	$1.865 \pm 0.016\%$
16_MU	0.02015 ± 0.00016	0.03746 ± 0.00009	$1.859 \pm 0.016\%$
17_MD	0.02185 ± 0.00017	0.04056 ± 0.00016	$1.857 \pm 0.016\%$
17_MU	0.02189 ± 0.00017	0.04009 ± 0.00015	$1.831 \pm 0.016\%$
18_MD	0.02120 ± 0.00017	0.03953 ± 0.00014	$1.864 \pm 0.016\%$
18_MU	0.02119 ± 0.00017	0.03938 ± 0.00016	$1.858 \pm 0.016\%$

Table 6: The weighted $\epsilon^{Rec\&Sel}$ for Λ_b and B_d^0 per year and polarization as well as the efficiency ratio.

5.3 Efficiency and uncertainty

The weights help to improve the quality of our simulation data even more. With this in mind the determination of the actual efficiency is pretty straight forward. We apply a passing criteria concerned with the efficiency we are calculating to a sample and count events before and after this selection criteria as can be seen in equation 26, where N is always the weighted number of events, and logically pass denotes the number of events that passed a cut, and fail denotes the number of events that fail to pass this cut.

$$\epsilon = \frac{N_{after}}{N_{before}} = \frac{N_{pass}}{N_{pass} + N_{fail}} \quad (26)$$

This method is absolutely fine to determine the efficiency. But we cannot naively use the weighted counts to determine the uncertainty of our sample. In equation 26 we see that the efficiency is calculated from the number of events that pass a selection divided by the number of events that pass a selection and that fail a selection. These N 's are correlated, so the propagation of the error on this efficiency is not straightforward. We can write the uncertainty on the efficiency as equation 27

$$\sigma\epsilon = \sqrt{\left(\frac{d\epsilon}{dN_p}\right)^2 \sigma N_p^2 + \left(\frac{d\epsilon}{dN_f}\right)^2 \sigma N_f^2} \quad (27)$$

If we replace the efficiencies of the right hand side of equation 27 by the definition of the efficiency given in equation 26 we get the results from equation 28 and 29.

$$\frac{d\epsilon}{dN_p} = \frac{d}{dN_p} \frac{N_p}{N_p + N_f} = \frac{-N_p}{(N_p + N_f)^2} + \frac{N_p + N_f}{(N_p + N_f)^2} \quad (28)$$

$$\frac{d\epsilon}{dN_f} = \frac{d}{dN_f} \frac{N_p}{N_p + N_f} = \frac{-N_p}{(N_p + N_f)^2} \quad (29)$$

substituting these back into equation 27 leaves us with equation 30 and finally with the resulting efficiency uncertainty in equation 31.

$$\sigma\epsilon = \sqrt{\frac{N_f^2 N_p + N_p^2 N_f}{(N_p + N_f)^2}} = \frac{\sqrt{N}}{N^2} \sqrt{N_f N_p} = \frac{\sqrt{N} \sqrt{(N - \epsilon N)(N \epsilon)}}{N^2} \quad (30)$$

$$\sigma\epsilon = \frac{\sqrt{N}}{N} \sqrt{\epsilon(1 - \epsilon)} \quad (31)$$

In equation 31 we have the uncertainty on the (weighted) efficiency, where N is the unweighted count of total events and ϵ is the weighted efficiency.

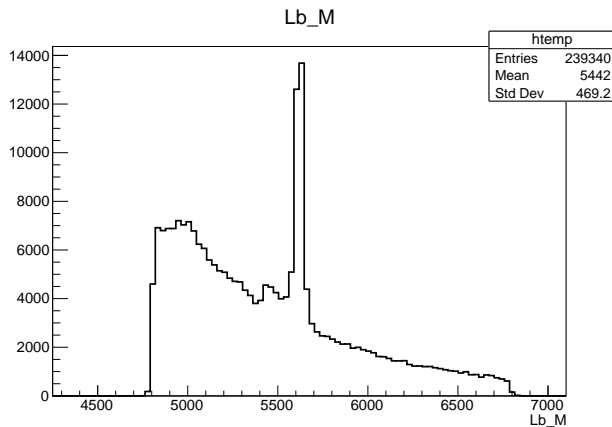


Figure 24: Here we see a mass spectrum after the stripping phase. We see a clear signal peak around the Λ_b^0 mass, as well as a peaking background and the combinatorial background.

6 Yield

This section describes the method used to extract the number of $\Lambda_b^0 \rightarrow \Lambda^0 J/\Psi$ and $B_d^0 \rightarrow K_s^0 J/\Psi$ decays from the invariant mass spectrum. The invariant mass spectrum is obtained from the collected data after selections are applied and it contains counts of our signal decays and background (decays) that look like our signal. Ultimately we want to construct a fitting model that describes the distribution of the invariant mass spectrum in data. This model consists of different probability density functions (pdf's), that describe the signal and background events in our invariant mass spectrum. The integral of the signal pdf will then give us the *yield*, or number of signal decays.

6.1 Invariant mass spectrum

An invariant mass spectrum depicts the number of detected decays that pass the selection criteria and can be reconstructed as a mother particle with a certain mass. Identifying the mother particle of a decay starts with assuming a "mass hypothesis" on the identified particles in an event. Together with information collected by the trackers on the momentum of these particles, the mass of the mother particle can be reconstructed. These reconstructed masses of the mother particles result in an invariant mass spectrum which contains signal and pollution from background events. In Figure 24 we can see such a spectrum, with a signal peak, a small background peak and combinatorial background.

Furthermore, although our mother particle (and mother particles of similar decays) do have a specific mass, the peaks in our spectrum are not delta peaks at this specific mass. Instead we have a gauss-like distribution of signal in our spectrum around the mass of our mother particle. This gauss-like distribution comes from the fact that the LHCb detector has a resolution, meaning that its accuracy is not infinitely large. This leads to an inaccuracy in the momenta of detected particles, that corresponds to the width in our peak.

In principle such a width in a particles mass peak could also be caused by the

short lifetime of a particle, that leads to a Breit-Wigner like peak.[9] However all particles that we are concerned with, meaning the mother Λ_b^0 and first daughters Λ^0 and J/Ψ , have a lifetime sufficiently large so that we can rule out this effect. This is despite the latter (J/Ψ) being on resonance, which is often an indication for an Breit-Wigner like mass peak.

The Gaussian shape of our signal distribution comes from the resolution of the detector, but the resolution is not the same for every event. This gives rise to additional features in the signal shape, that we will encounter in our fit. Effectively it means that the tails of our signal shape are smeared out more than for a normal Gaussian. Furthermore random scattering of particles in the detector causes momentum loss, which gives rise to an enhanced tail to the left of our mass peaks.

6.2 Maximum Likelihood Fit

To determine the yield of our decay, we make use of the method of maximum likelihood in RooFit. We fit functions to Monte Carlo data for our signal shape and all peaking backgrounds. We combine this with a function for the combinatorial background to a normalized parametrical model that describes our invariant mass spectrum. Understanding and correct modelling of these shapes is crucial and the method to do this is described below.

For our fit we decided to use a Monte Carlo background selection cut. Here we remove a category of events from our simulated data that pass the truth matching, but still contains both some real candidates and some false candidates. Furthermore we use our knowledge of the expected shapes of signal and background in our invariant mass spectrum to pick suitable functions.

6.3 Λ_b^0 Signal shape

The method to determine the Signal shape of the Λ_b^0 is similar to the method to find the shape of the peaking background. We use MC data of our signal that has passed all stripping and selection and fit a probability density function to the resulting mass spectrum. As described above the distribution of events is Gauss like with a tail on both sides of the peak. We found that this peak is best fit with a Hypatia[37] with two tails, as given in equation 33 and 32.[38]

$$\text{Hypatia2} = f(x; \mu, \sigma, \lambda, \zeta, \beta, a_l, n_l, a_r, n_r) \quad (32)$$

$$\text{Hyp} = \begin{cases} \frac{G(\mu - a_l \sigma, \mu, \sigma, \lambda, \zeta, \beta)}{\left(1 - \frac{x}{n_l G(\mu - a \sigma, \mu, \sigma, \lambda, \zeta, \beta)} / G'(\mu - a \sigma, \mu, \sigma, \lambda, \zeta, \beta) - a_l \sigma\right)^{n_l}}, & \frac{x - \mu}{\sigma} < -a_l \\ \left((x - \mu)^2 + A_\lambda^2(\zeta) \sigma^2 \right)^{\frac{1}{2} \lambda - \frac{1}{4}} e^{\beta(x - \mu)} K_{\lambda - \frac{1}{2}} \left(\zeta \sqrt{1 + \left(\frac{x - \mu}{A_\lambda(\zeta) \sigma} \right)^2} \right), & \text{otherwise} \\ \frac{G(\mu + a_r \sigma, \mu, \sigma, \lambda, \zeta, \beta)}{\left(1 - \frac{x}{n_r G(\mu - a \sigma, \mu, \sigma, \lambda, \zeta, \beta)} / G'(\mu - a \sigma, \mu, \sigma, \lambda, \zeta, \beta) - a_r \sigma\right)^{n_r}}, & \frac{x - \mu}{\sigma} > -a_r \end{cases} \quad (33)$$

$$A_\lambda^2(\zeta) = \frac{\zeta K_\lambda(\zeta)}{K_{\lambda+1}(\zeta)} \quad (34)$$

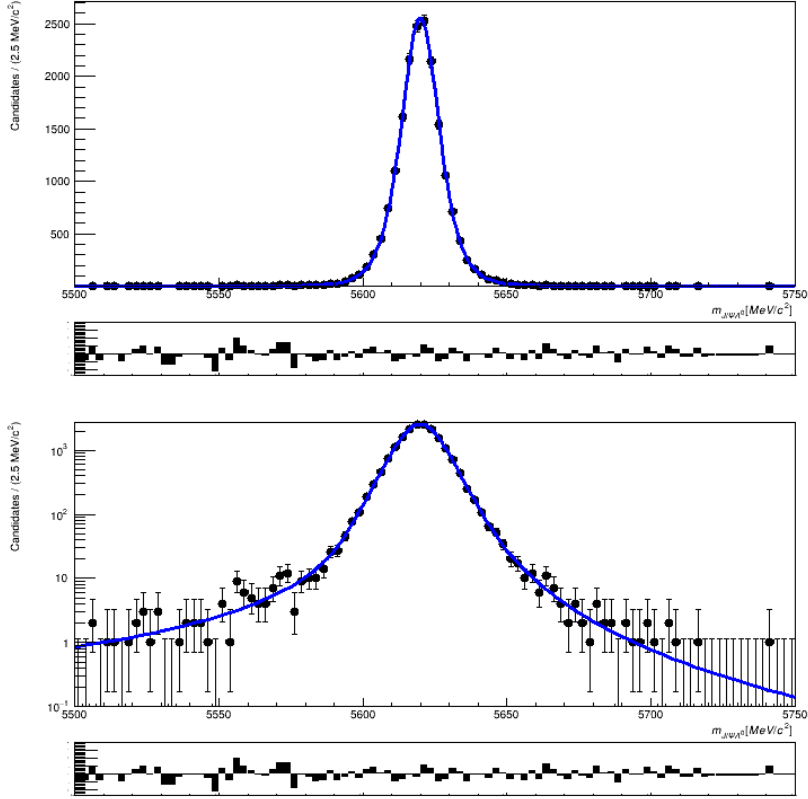


Figure 25: A regular (top) and a log (bottom) plot of the fit of the Hypatia shape to the Monte Carlo data.

In equation 32, 33 and 34 G is a limit case of the generalized hyperbolic distribution and G' its derivative. K_λ are the modified Bessel functions of the second kind, μ is the mean, σ is the standard deviation, a_l and a_r are the start of the left and right tail respectively, n_l and n_r are the shape parameters of the left and right tail respectively.

Once we reach $\frac{x-\mu}{\sigma} < -a_l$ or $\frac{x-\mu}{\sigma} > a_r$ the Hypatia has a power-law-like behaviour, for the rest it is gauss-like. To fit this function to the MC data we fix the Skewness parameter β and the per event error distribution parameters λ and ζ .

After a successful fit, that can be seen in Figure 25, we fix a_l, a_r, n_l and n_r and use the shape with a free (within boundary) μ and σ as the Signal shape in our final model.

6.4 B_d^0 Signal shape

To find the signal shape of the normalization channel we also use a Hypatia with two tails and fit this to MC data. As for the Λ_b , we set a constant λ, ζ and β before fitting the function to the MC data. After a successful fit, that

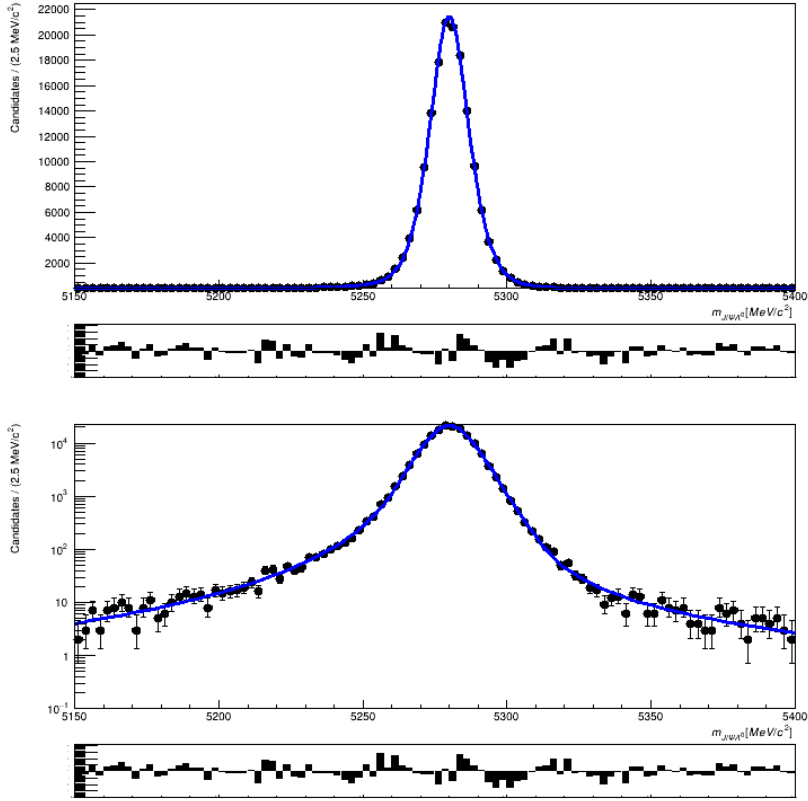


Figure 26: A regular (top) and a log (bottom) plot of the fit of the Hypatia shape to the Monte Carlo data.

can be seen in Figure 26 we set a_l, a_r, n_l and n_r constant. Furthermore we set the mean of the B_s shape to have the value of the mean of the signal shape +86 (MeV). We then add this signal shape to the final model for the normalization channel with all fixed parameters except for the μ and σ of the signal shape.

6.5 Backgrounds

We have described why we find a peak with a width and not a delta peak at a particles mass, but there's more physics hidden in the spectrum. The most prominent feature is the combinatorial background, a so called *non peaking background* as it is present throughout the whole mass window of the spectrum. The combinatorial background consists of random tracks of particles that pass the trigger and stripping lines and can be combined to resemble our sought after decay.

Furthermore there is *peaking background* that can come from either partially reconstructing a decay, or misidentifying a particle. With partial reconstruction, we fail to detect a particle in the background decay, making it look like our decay. Misidentification happens when one of the daughter particles passes the mass cuts with a signal mass hypotheses, making it look like our target decay.

The J/Ψ is no source of physics background, as this is identified through two well detectable muons. Therefore, any peaking background must come from misidentification of a hadron in the final state, or a missing particle.

6.5.1 Combinatorial Background Shape

One of the biggest tasks of the analyst is often to reduce the combinatorial background as much as possible, while optimising the relative uncertainty on the yield. Completely removing the combinatorial background is usually not possible, so it has to be incorporated into the fit. This means that we need to have some information on the combinatorial background, which is an important reason to ensure the mass window contains only combinatorial on the left- and right-hand side. The combinatorial background is present in both our signal and normalization channel.

The fit model for the combinatorial background shape has the simplest form out of the three models. This background is most prominent in lower ranges of the mass spectrum and its contribution gradually decreases towards the heavier end of the spectrum. We can use an exponential with a single exponential parameter with arbitrary normalization. We use an exponential in both the signal and the normalization channel fits.

6.5.2 Peaking Background Shape for Λ_b^0

The Λ^0 in our signal has a relative large lifetime, so that only decays involving strange hadrons like K_s^0 , Ξ^0 and Ω^0 can mimic the decay. The only significant peaking background comes from the $B^0 \rightarrow J/\Psi K_s^0$ decay, which happens to be our normalization channel. Other decays are negligible because of a much smaller branching ratio or a peak far away from ours.[27]

For $B^0 \rightarrow J/\Psi K_s^0$ a π^\pm from the decay of the K_s^0 can be misidentified as a p . This causes the reconstructed mass of the mother particle to be in the region of our signal peak. We will see that we can fit this background nicely from simulated data, and so account for it in our total fit. The slightly heavier B_s^0 meson can via the same miss-identification enter our spectrum, however this decay is Cabibbo suppressed by approximately a factor 100 and therefore ignored.

The peaking background from $B^0 \rightarrow J/\Psi K_s^0$ in the $\Lambda_b^0 \rightarrow J/\Psi \Lambda^0$ fit, is fitted by a Crystal Ball Function, to deal its non Gaussian nature. The Crystall Ball Function consist of a Gaussian core, with a power-law tail and is given by equation 35:[32]

$$f(x; \alpha, n, \bar{x}, \sigma) = N \cdot \begin{cases} \exp\left(-\frac{(x-\bar{x})^2}{2\sigma^2}\right), & \text{for } \frac{x-\bar{x}}{\sigma} > -\alpha \\ A \cdot \left(B - \frac{x-\bar{x}}{\sigma}\right)^{-n}, & \text{for } \frac{x-\bar{x}}{\sigma} \leq -\alpha \end{cases} \quad (35)$$

where

$$A = \left(\frac{n}{|\alpha|}\right)^n \cdot \exp\left(-\frac{|\alpha|^2}{2}\right),$$

$$B = \frac{n}{|\alpha|} - |\alpha|,$$

It has four parameters $(\alpha, n, \bar{x}, \sigma)$, where \bar{x} is the mean of the Gauss, σ

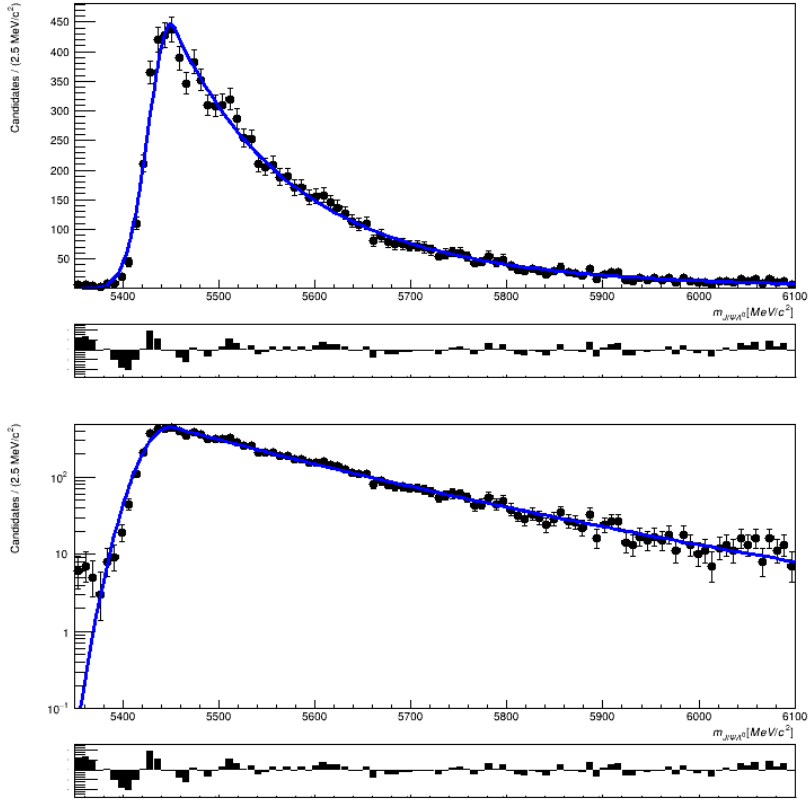


Figure 27: A regular (top) and a log (bottom) plot of the fit of the Hypatia shape to the Monte Carlo data.

its standard deviation, α determines where the power-law part takes over from the Gaussian part and n determines the shape of the power-law tail. N is the normalization factor.

To determine the shape of the model (the value of the parameters), we fit simulated B_d^0 events that have passed the same stripping and selection as our CL data.

We can see a result of this fit in Figure 27. The parameters found in this MC fit are fixed for the final fit, so that only its yield can vary in the final fit to the data.

6.5.3 Peaking Background Shape for B_d^0

The decays that play a role in the normalization spectrum are very similar to the signal spectrum. We have some background from the $\Lambda_b^0 \rightarrow \Lambda^0 J\Psi$ on the right side of our peak in the normalization channel. The inverse happens here, the final state proton can be misidentified as a pion, which makes it look like the normalization decay.

Furthermore, the B_s^0 plays a more important role in this spectrum, as the final state particles are the same as for the B_d^0 decay. However, as mentioned

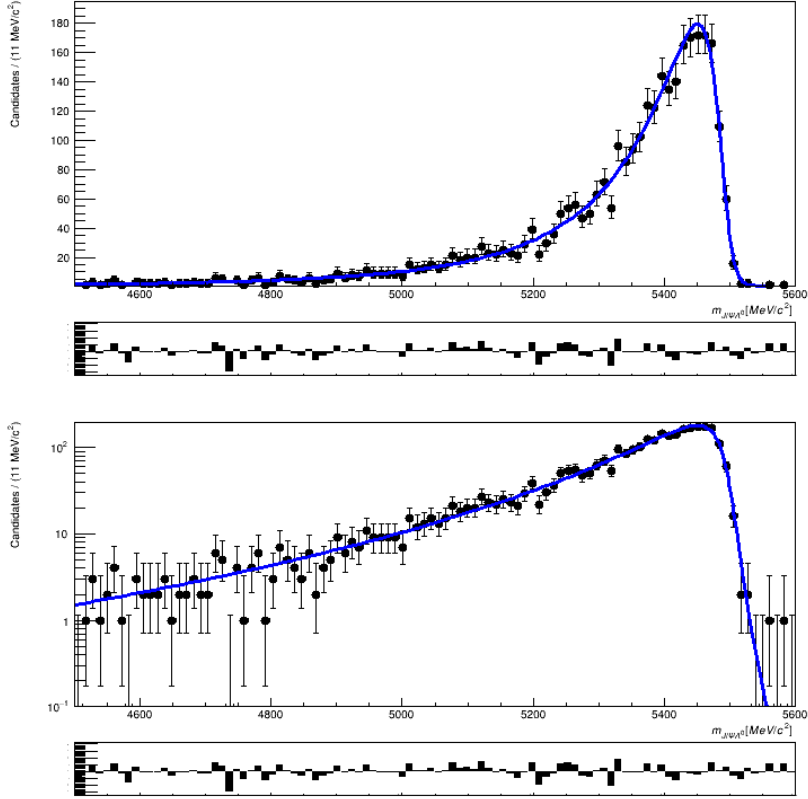


Figure 28: A regular (top) and a log (bottom) plot of the fit of the Hypatia shape to the Monte Carlo data.

above, this decay is much less abundant due to Cabibbo suppression.

The $\Lambda_b^0 \rightarrow \Lambda^0 J/\Psi$ peaking background has its peak on the right side of our normalization decay, but a tail that runs under the peak of our B_d^0 decay. To model this peaking background, we use a Johnson probability density function, as given in equation 36[33]

$$f(x; \mu, \lambda, \gamma, \delta) = \frac{\delta}{\lambda\sqrt{2\pi}} \frac{1}{\sqrt{1 + \left(\frac{x-\mu}{\lambda}\right)^2}} \exp\left[-\frac{1}{2}\left(\gamma + \delta \sinh^{-1}\left(\frac{x-\mu}{\lambda}\right)\right)\right] \quad (36)$$

where μ is the mean of the distribution, λ is the standard deviation, γ is the skewness(determines the asymmetry of the pdf), and δ is the kurtosis (the ratio between tail and peak) for the pdf. We fit this function to MC data to get the right shape as can be seen in Figure 28.

We fix the resulting parameters for the final fit.

The B_s can decay to exactly the same final state particles and is therefore present in our mass spectrum. Since the B_s is slightly heavier than the B_d^0 this peak shows up on the right side of our normalization peak. Since the decay looks similar to the B_d^0 shape we inherit the Hypatia shape that we use for the B_d^0 , and fix the parameters for the final model.

6.6 Total fit shapes

$\Lambda_b^0 \rightarrow \Lambda^0 J/\Psi$ In the final model for the signal channel we have a combination of a Hypatia (Signal), Double sided Crystal Ball (B_d^0) and an Exponential (Combinatorial). The free parameters are μ and σ of the Hypatia, as well as the yield fractions of the three pdfs.

$B_d^0 \rightarrow K_s^0 J/\Psi$ In the final model for the normalization channel we have a combination of a Hypatia (Signal), another Hypatia (B_s), Johnson (Λ_b^0) and an Exponential (Combinatorial). The free parameters are μ and σ of the Signal Hypatia, as well as the yield fractions of the three pdfs.

6.6.1 Resulting Yield

The resulting Model fits are shown in Figures 29, 30, 31 and 32. While the resulting Yield can be found in Table 7 and 8.

	$N_{\Lambda_b^0 \rightarrow \Lambda^0 J/\Psi}$	Uncertainty(%)
16_MD	3637 ± 71	1.95%
16_MU	3278 ± 68	2.06%
17_MD	4002 ± 74	1.85%
17_MU	3694 ± 70	1.9%
18_MD	4471 ± 78	1.74%
18_MU	4873 ± 81	1.66%

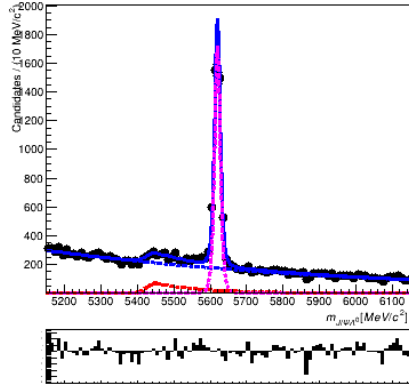
Table 7: $\Lambda_b^0 \rightarrow \Lambda^0 J/\Psi$ Yield with uncertainty and the relative uncertainty

	$N_{B_d^0 \rightarrow K_s^0 J/\Psi}$	Uncertainty(%)
16_MD	19292 ± 153	0.79%
16_MU	17863 ± 147	0.82%
17_MD	21203 ± 159	0.75%
17_MU	19488 ± 152	0.78%
18_MD	24464 ± 171	0.7%
18_MU	26144 ± 177	0.68%

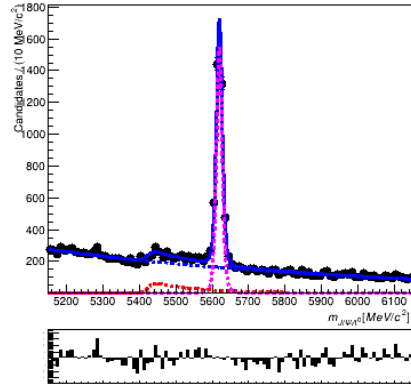
Table 8: $B_d^0 \rightarrow K_s^0 J/\Psi$ Yield with uncertainty and the relative uncertainty

6.6.2 Systematic Uncertainties

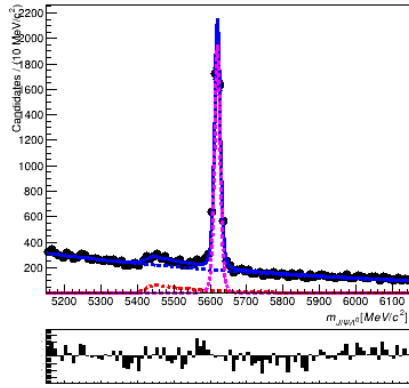
To account for uncertainties in the fit model we have also done the full fitting procedure with a Double Sided Crystal Ball instead of a Hypatia. (for the B_d^0 spectrum, this means that the B_s shape inherits the Double Sided Crystal Ball shape from the signal shape) The difference between these models have been used to set a systematic error, which is presented in chapter 7.



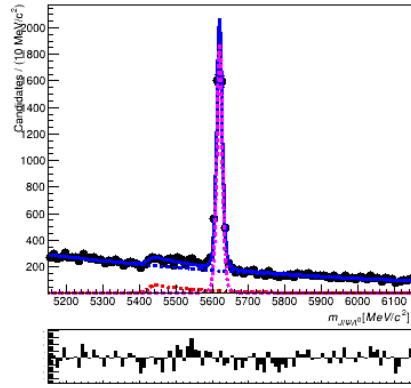
(a) 2016MD $\Lambda_b^0 \rightarrow \Lambda^0 J/\Psi$



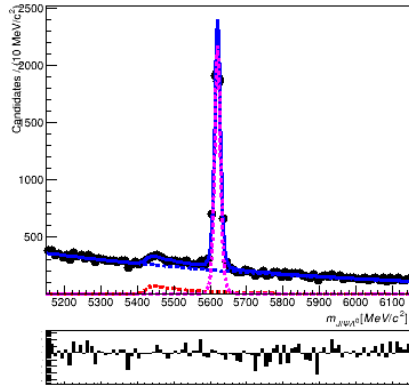
(b) 2016MU $\Lambda_b^0 \rightarrow \Lambda^0 J/\Psi$



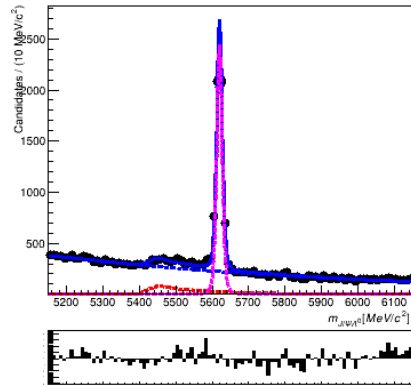
(c) 2017MD $\Lambda_b^0 \rightarrow \Lambda^0 J/\Psi$



(d) 2017MU $\Lambda_b^0 \rightarrow \Lambda^0 J/\Psi$

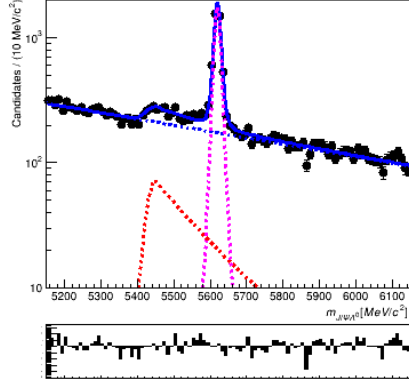


(e) 2018MD $\Lambda_b^0 \rightarrow \Lambda^0 J/\Psi$

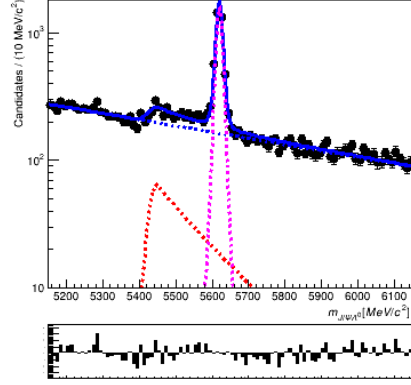


(f) 2018MU $\Lambda_b^0 \rightarrow \Lambda^0 J/\Psi$

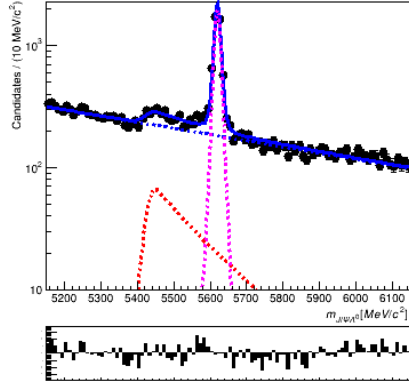
Figure 29: Plots of the fitted invariant mass spectrum. The black dots are databins, the blue line is the complete fit model, the blue dotted line is the combinatorial background shape, the dotted purple line is the signal shape and the red line is the peaking background shape.



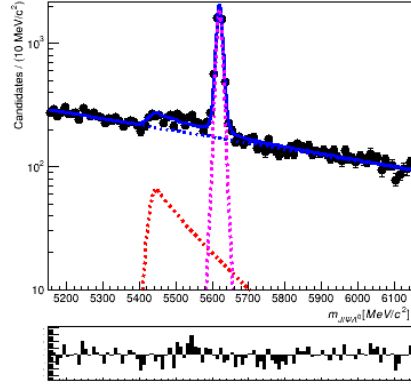
(a) 2016MD $\Lambda_b^0 \rightarrow \Lambda^0 J/\Psi$



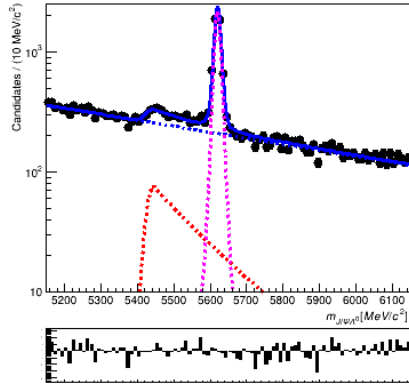
(b) 2016MU $\Lambda_b^0 \rightarrow \Lambda^0 J/\Psi$



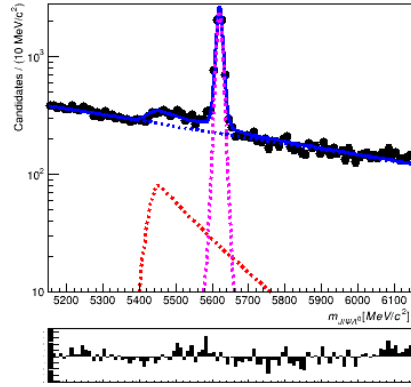
(c) 2017MD $\Lambda_b^0 \rightarrow \Lambda^0 J/\Psi$



(d) 2017MU $\Lambda_b^0 \rightarrow \Lambda^0 J/\Psi$

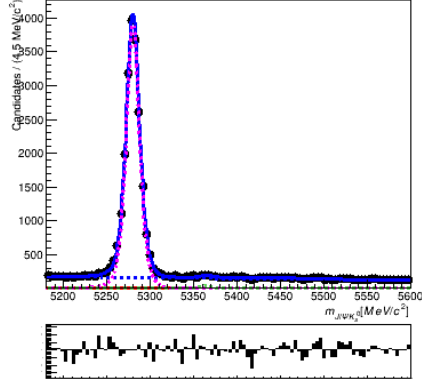


(e) 2018MD $\Lambda_b^0 \rightarrow \Lambda^0 J/\Psi$

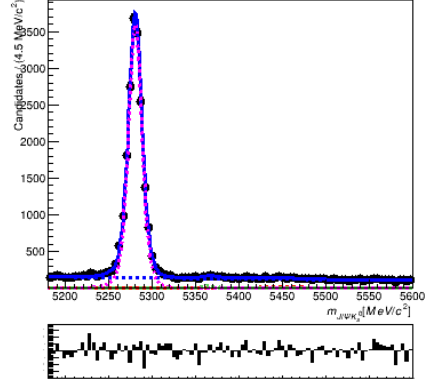


(f) 2018MU $\Lambda_b^0 \rightarrow \Lambda^0 J/\Psi$

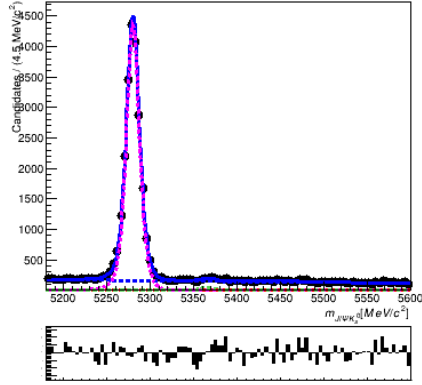
Figure 30: Log-scale plots of the fitted invariant mass spectrum. The black dots are databins, the blue line is the complete fit model, the blue dotted line is the combinatorial background shape, the dotted purple line is the signal shape and the red line is the peaking background shape.



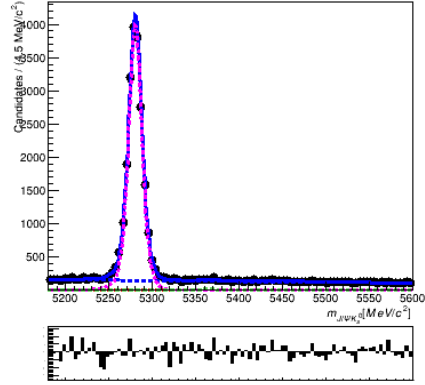
(a) 2016MD $B_d^0 \rightarrow K_s^0 J/\Psi$



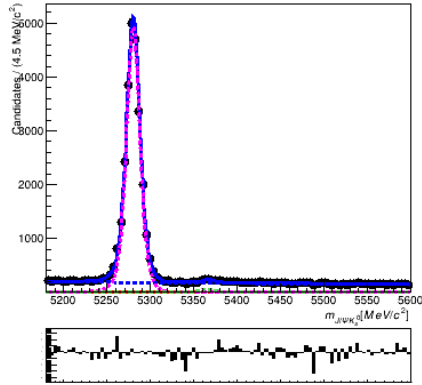
(b) 2016MU $B_d^0 \rightarrow K_s^0 J/\Psi$



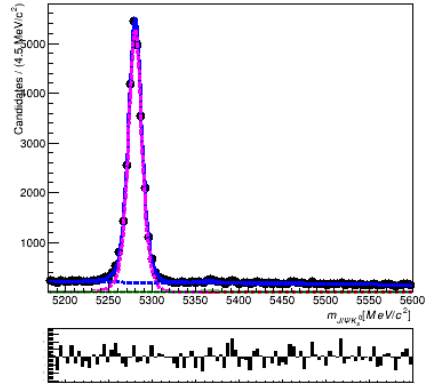
(c) 2017MD $B_d^0 \rightarrow K_s^0 J/\Psi$



(d) 2017MU $B_d^0 \rightarrow K_s^0 J/\Psi$

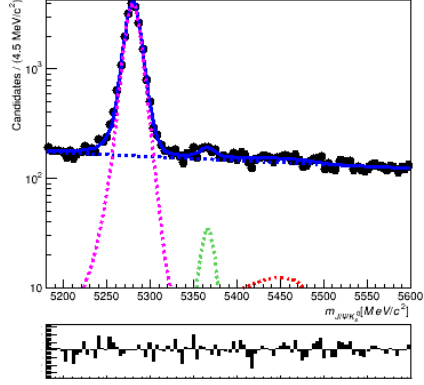


(e) 2018MD $B_d^0 \rightarrow K_s^0 J/\Psi$

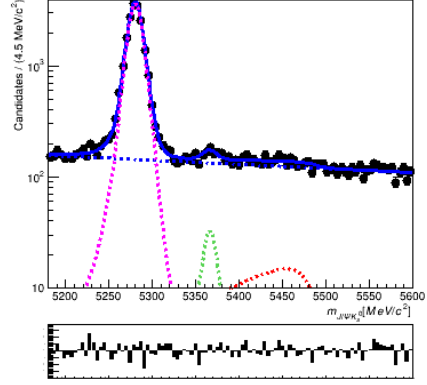


(f) 2018MU $B_d^0 \rightarrow K_s^0 J/\Psi$

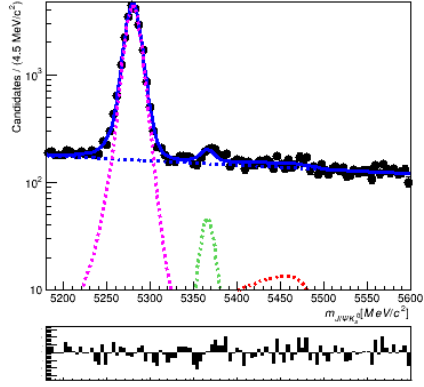
Figure 31: Plots of the fitted invariant mass spectrum. The black dots are databins, the blue line is the complete fit model, the blue dotted line is the combinatorial background shape, the dotted purple line is the signal shape, the dotted green line is the B_s shape and the dotted red line is the Λ_b^0 shape..



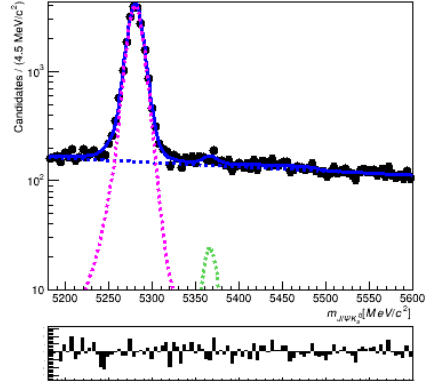
(a) 2016MD $B_d^0 \rightarrow K_s^0 J/\Psi$



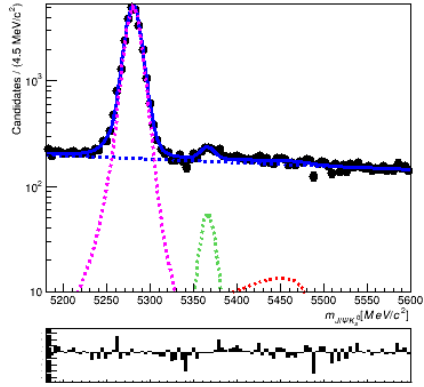
(b) 2016MU $B_d^0 \rightarrow K_s^0 J/\Psi$



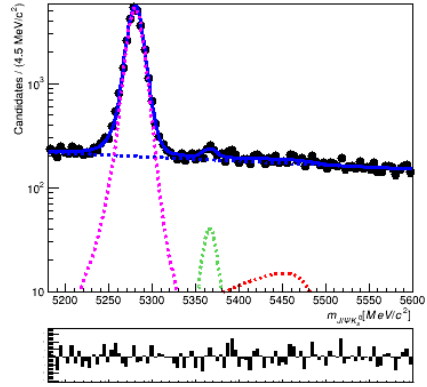
(c) 2017MD $B_d^0 \rightarrow K_s^0 J/\Psi$



(d) 2017MU $B_d^0 \rightarrow K_s^0 J/\Psi$



(e) 2018MD $B_d^0 \rightarrow K_s^0 J/\Psi$



(f) 2018MU $B_d^0 \rightarrow K_s^0 J/\Psi$

Figure 32: Log-scale plots of the fitted invariant mass spectrum. The black dots are databins, the blue line is the complete fit model, the blue dotted line is the combinatorial background shape, the dotted purple line is the signal shape, the dotted green line is the B_s shape and the dotted red line is the Λ_b^0 shape.

7 Systematic Uncertainties

Systematic uncertainties are those that can be attributed to uncertainties in the method used. Therefore they differ from statistical errors. The methods discussed here are the weights we use for the calculation of the efficiency and the model we use for the fit.

We have seen before that we can make use of the fact that we measure a ratio of a branching fraction ratio, and this is also the case here. Any method that we use may bring it with an uncertainty, but since most of the methods are applied to both channels, the effect can partly cancel out.

7.1 Systematic uncertainties of the efficiency

The first systematic uncertainty we add is for the efficiency. As discussed in chapter 5, we make use of weights to determine the efficiency. We apply these weights because we think this will result in a more accurate efficiency calculation. However, this is a choice of method, and therefore it comes with an uncertainty.

To estimate the systematic uncertainty of the method, we use a similar approach as for the fit model. We calculate the efficiency with and without the weight applied and use the difference to estimate an uncertainty. We will most likely get an overestimation of the actual systematic uncertainty as we think our method to determine the efficiency is the most accurate.

Since the weights are correlated, we get the best estimation by determining a uncertainty for all weights separately. We can once again make use of the ratio of the branching fractions, but not for all weights. Out of the five weights we apply, two are only relevant for the Λ_b^0 -decay, and thus they directly affect the result.

Furthermore, we have to consider two separate uncertainties for the efficiency up to the stripping and the efficiency from the stripping to the final selection, as we use different methods to calculate these efficiencies. To calculate the uncertainty on the efficiency we use the following equation,

$$\epsilon_{uncertainty} = \left(\frac{\frac{\epsilon_{B_d^0}^{unweighted}}{\epsilon_{B_d^0}^{weighted}}}{\frac{\epsilon_{\Lambda_b^0}^{unweighted}}{\epsilon_{\Lambda_b^0}^{weighted}}} - 1 \right) * 100\% \quad (37)$$

Here the superscript depicts the value without one of the weights (unweighted) or with all weights applied (weighted). The subscripts B_d^0 and Λ_b^0 stand for the decay channel. If we apply this to all five weights, and for all datasets we get the results as shown in tables 9 and 10.

7.2 Systematic uncertainties of the fit model

The fit model consists of a combination of background shapes and the signal shape. For the Λ_b^0 -model, we have a total of 3 shapes. For the B_d^0 -model, we have 4 shapes in total. For both models we use a Hypatia as the signal shape. To determine a systematic uncertainty for the shape of the model we

use a different shape for the signal. We use the difference between the result of the Hypatia shape and the Double Sided Crystal ball shape as an estimate of the systematic uncertainty of the model.

Since we have carefully selected our Hypatia Shape as the best fit for our signal, this difference is likely an overestimation of our actual systematic uncertainty. In principle, we could also test the model with different shapes for the background. However, the signal shape makes up the largest part of our model, so the uncertainties on the fit shape of the background would be negligible compared to those on the signal shape.

For the B_d^0 -model, we use the same shape for the signal and the small B_s^0 -background shape. Therefore, we also alter the shape of the B_s -shape while running the fit with the Double Sided Crystal Ball shape. If we perform the fitting procedure with both shapes we can determine the yield and combine this into an estimate of the uncertainty of the ratio as a percentage for all data-sets as shown in equation 38

$$Fit\ Uncertainty = \left(\frac{\frac{Yield_{\Lambda_b}^{DCB}}{Yield_{\Lambda_b}^{Hyp}}}{\frac{Yield_{B_d^0}^{DCB}}{Yield_{B_d^0}^{Hyp}}} - 1 \right) * 100\% \quad (38)$$

Here the superscript DCB stands for the Yield with the Double Sided Crystal Ball shape, and the superscript stands for the Yield with the Hypatia Shape. The subscripts Λ_b and B_d^0 stand for their respective decay channels. This finally results in an estimated relative systematic fit model uncertainty on the

	MD16	MU16	MD17	MU17	MD18	MU18
Tracking	0.02%	0.02%	-0.06%	-0.08%	-0.08%	-0.09%
Kinematic	-4.67%	-4.78%	-4.05%	-3.65%	-4.61%	-4.42%
Λ_b -lifetime	0.54%	0.54%	0.53%	0.52%	0.54%	0.53%
Λ_b -ang distr	2.97%	2.95%	3.38%	3.6%	3.12%	3.01%
PID	0.14%	0.16%	0.05%	0.06%	0.06%	0.06%

Table 9: Relative Systematic Uncertainty ϵ^{Sel} on Ratio

	Kinematic	Λ_b-lifetime	Λ_b-ang distr
MD	-2.03%	0.00%	0.02%
MU	-2.00%	0.00%	0.01%

Table 10: Relative Systematic Uncertainty ϵ^{Rec} on Ratio

MD16	MU16	MD17	MU17	MD18	MU18
-0.63%	-1.02%	-0.42%	-0.38%	-0.54%	0.6%

Table 11: Relative Systematic Uncertainty Fit Shape on Ratio in percentage of the Yield Ratio

branching fraction ratio as given in Table 11

8 Results

Finally to find the $BR(\Lambda_b^0 \rightarrow \Lambda^0 J/\Psi)$ we have to combine our Efficiencies, Yield, (Systematic) Uncertainties and the external production factor and branching fraction of our normalization channel. Both production factor and branching fraction have a single value with its uncertainty. The Efficiencies, Yield and Uncertainties have separate values for each dataset and therefore have to be combined into a single expression. We use our efficiency as a weight to combine the results for different datasets.

8.1 Efficiency Corrected Yield Ratio

To determine the Branching Fraction of $\Lambda_b^0 \rightarrow \Lambda^0 J/\Psi$ we can rewrite Equation 3 to Equation 39

$$BR(\Lambda_b^0 \rightarrow \Lambda^0 J/\Psi(\mu^+ \mu^-)) = \frac{1}{BR(B^0 \rightarrow K_s^0 J/\Psi(\mu^+ \mu^-))} \left(\frac{f_{\Lambda_b^0}}{f_d}\right)^{-1} \alpha, \quad (39)$$

Where α is the Efficiency Corrected Yield Ratio given in Equation 40

$$\alpha = \frac{\frac{N_{sig}}{\epsilon_{sig}}}{\frac{N_{norm}}{\epsilon_{norm}}} \quad (40)$$

To define the total Efficiency Corrected Yield Ratio we use equation 41 and 42

$$\bar{x} = \sigma_{\bar{x}}^2 \sum_{i=1}^n \frac{x_i}{\sigma_i^2}, \quad (41)$$

$$\sigma_{\bar{x}} = \sqrt{\frac{1}{\sum_{i=1}^n \sigma_i^{-2}}}. \quad (42)$$

Where \bar{x} is the Weighted Yield ratio, $\sigma_{\bar{x}}$ is the Weighted Yield Ratio Uncertainty, x_i and σ_i are the Yield Ratio and Uncertainty respectively where i depicts the six data sets we collected.

This results in an Efficiency Corrected Yield Ratio of 0.097 ± 0.00079 . Here the uncertainty is the statistical uncertainty. We can find the resulting Systematic Uncertainties and External Systematic Uncertainties in Table 12 and 13.

We can combine the uncertainties to find our final result for the branching fraction,

$$BR(\Lambda_b^0 \rightarrow \Lambda^0 J/\Psi(\mu^+ \mu^-)) = 3.63 \pm 0.03 \pm 0.20 \pm 0.27 \cdot 10^{-4}$$

Where the first uncertainty is of statistical nature, the second of systematic nature and the third comes from external input.

	Uncertainty (%)
Kinematic Weight	-4.4%
$\tau_{\Lambda_b^0}$ Weight	0.5%
Λ_b^0 Angular Weight	3.2%
Tracking Weights	-0.0%
PID Weight	0.0%
Efficiency Ratio	0.6%
Fit Shapes	-0.4%

Table 12: Relative Systematic Uncertainty per Contributing Method.

	Uncertainty
$\frac{f_{\Lambda_b^d}}{f_d}$	$-0.25 \cdot 10^{-4}$
$\text{BR}(B_d^0 \rightarrow K_s^0 J/\Psi)$	$0.09 \cdot 10^{-4}$
$\text{BR}(\Lambda^0 \rightarrow p\pi)$	$0.02 \cdot 10^{-4}$
$\text{BR}(K_s^0 \rightarrow \pi^-\pi^+)$	$0.00 \cdot 10^{-4}$

Table 13: Absolute Systematic Uncertainty per External input.

9 Discussion

We have presented the first LHCb analysis of the determination of the $\Lambda_b^0 \rightarrow \Lambda^0 J/\Psi$ branching fraction. Furthermore this is the first determination of $\text{BR}(\Lambda_b^0 \rightarrow \Lambda^0 J/\Psi)$ with an accurate $\frac{f_{\Lambda_b^0}}{f_d}$. This measurement improves the uncertainty of the previously best known branching fraction with a factor 3. The measured branching fraction is consistent with previous measurements.

We find that an improved accuracy of the measured value of the branching fraction does not depend on statistics. The dominant factor is the LHCb production factor ratio. An improved measurement of the production factor could decrease the uncertainty of the $\text{BF}(\Lambda_b^0 \rightarrow \Lambda^0 J/\Psi)$.

Furthermore we note that we have used a conservative estimation of our systematic uncertainties due to weights. Finding a method to find an accurate but less conservative estimate of these systematic uncertainties can help to lower the uncertainty on the $\text{BF}(\Lambda_b^0 \rightarrow \Lambda^0 J/\Psi)$.

References

- [1] Patrignani, C. et al. [Particle Data Group], 2016, (and 2017 update). "Review of Particle Physics." *Chinese Physics C* 40, 100001.
- [2] Kuindersma, H. 2018. *Detecting Muons at LHCb Upgrade Conditions*. Unpublished master thesis, University of Groningen.
- [3] Kuindersma, H. 2016. *Trigger Efficiencies at LHCb in the Search for $B_s^0 \rightarrow e^\pm \mu^\mp$* . Unpublished bachelor thesis, University of Groningen.
- [4] Tolk, S. 2016. *Discovery of Rare B Decays*. PhD thesis, University of Groningen.
- [5] Aaij, R. et al., [LHCb Collaboration], 2019. "Design and performance of the LHCb trigger and full real-time reconstruction in Run 2 of the LHC." *Jinst* 14, P04013.
- [6] Koopman, R. 2015. *Ageing of the LHCb outer tracker & b-hadron production and decay at $\sqrt{s} = 7$ TeV*. PhD thesis, University of Amsterdam.
- [7] Wiersema, G.S.P. 2017. *Using the $B^0 \rightarrow K^\pm \pi^\pm$ channel as normalization in the search for the charged lepton flavor violating $B_{(s)}^0 \rightarrow e^\pm \mu^\mp$ decay*. Unpublished master thesis, University of Groningen, 2017.
- [8] Albrechts, J. [LHCb Collaboration], 2018. *Lepton Flavour Universality tests with B decays at LHCb*. Contribution to the proceedings of the 53th Rencontres de Moriond, QCD Session, 17-24 March 2018.
- [9] Bettini, A. 2014. *Introduction to Elementary Particle Physics*. Cambridge University Press.
- [10] Martin, B.G. and G. Shaw. 2004 *Particle Physics*. John Wiley and Sons.
- [11] Martin, B. 2009. *Nuclear and Particle Physics*. John Wiley and Sons Ltd.
- [12] Neutrino dark energy and leptogenesis with TeV scale triplets - Scientific Figure on ResearchGate. Available from: https://www.researchgate.net/figure/The-tree-level-left-and-one-loop-right-decay-diagrams-for-x-1-1-A-lepton_fig2_283762532 [accessed 24 Jan, 2019]
- [13] Aaij, R. et al., [LHCb Collaboration], 2014. *Physical Review Letters*. 113.
- [14] Berendsen, H.J.C. 1997. *Goed Meten met Fouten*. Rug Bibliotheek.
- [15] Fajfer, Svjetlana, Jernej F. Kamenik, and Ivan Nišnjak, 2012. " $B \rightarrow D^* \tau \nu_\tau$ sensitivity to new physics." *Physical Review D* 85, 094025.
- [16] Corti, G et al., [LHCb Collaboration], 2015. "How the Monte Carlo production of a wide variety of different samples is centrally handled in the LHCb experiment." *Journal of Physics: Conference Series* Volume 664, Offline software.

- [17] Belyaev, I et al., [LHCb Collaboration], 2011. "Handling of the generation of primary events in Gauss, the LHCb simulation framework." *Journal of Physics: Conference Series* Volume 331, Issue 3.
- [18] Aaij, R. et al., [LHCb Collaboration], 2017. "Measurement of the $B_s^0 \rightarrow \mu^+\mu^-$ branching fraction and effective lifetime and search for $B^0 \rightarrow \mu^+\mu^-$ decays." *Physical Review Letters* 118, 191801.
- [19] Belyaev, Ivan, Victor Egorychev, Viacheslav Matiunin, Ivan Polyakov, 2018. *Observation of the $\Lambda_b^0 \rightarrow \Psi(2S)p\pi^-$ decay.* LHCb-ANA-2017-066.
- [20] Lazzeroni, C. N. Watson, M. Kreps, 2013. *Measurement of $\Lambda_b^0 \rightarrow \Lambda\mu^+\mu^-$ differential branching fraction.* LHCb-ANA-2011-094.
- [21] Aaij, R. et al., [LHCb Collaboration], 2019. "Measurement of the ratio of branching fractions of the decays $\Lambda_b^0 \rightarrow \Psi(2S)\Lambda^0$ and $\Lambda_b^0 \rightarrow J/\Psi\Lambda^0$." *Journal of High Energy Physics* 126.
- [22] Aaij, R. et al., [LHCb Collaboration], 2018. "Search for lepton-flavour-violating decays of Higgs-like bosons." *The European Physical Journal C* 78.
- [23] Aaij, R. et al., [LHCb Collaboration], 2017. "Measurement of B_s^0 and D_s^- meson lifetimes." *Physical Review Letters* 119, 101801.
- [24] Aaij, R. et al., [LHCb Collaboration], 2018. "Search for the lepton-flavour violating decays $B_{(s)}^0 \rightarrow e^\pm\mu^\mp$." *Journal of High Energy Physics* 78.
- [25] Aaij, R. et al., [LHCb Collaboration], 2019. "Design and performance of the LHCb trigger and full real-time reconstruction in Run 2 of the LHC." *Journal of Instrumentation* 14.
- [26] Paterno, Marc, and Fermilab, 2004. *Calculating efficiencies and their uncertainties.* United States. doi:10.2172/15017262. <https://www.osti.gov/servlets/purl/15017262>.
- [27] Mackowiak, Patrick, Vanessa Müller, Ramon Niet, Julian Wishahi, 2019. *Measurement of the ratio of branching fractions of the decays $\Lambda_b^0 \rightarrow \Psi(2S)\Lambda^0$ and $\Lambda_b^0 \rightarrow J/\Psi\Lambda^0$.* LHCb-ANA-2017-011.
- [28] Chilikin, K. et al., [Belle Collaboration], 2019. "Evidence for $B^+ \rightarrow h_c K^+$ and observation of $\eta_c(2S) \rightarrow p\bar{p}\pi^+\pi^-$ " *Physical Review D* 100, 1.
- [29] Zyla, P.A. et al., [Particle Data Group], 2020. "The Review of Particle Physics." To be published in *Progress of Theoretical and Experimental Physics* 083C01.
- [30] Olive, K.A. et al., [Particle Data Group], 2014. "Review of Particle Physics." *Chinese Physics C* 38, 090001.
- [31] Beringer, J. et al., [Particle Data Group], 2012c (and 2013 partial update for the 2014 edition). "Review of Particle Physics." *Physical Review D* 86, 010001.

- [32] https://en.wikipedia.org/wiki/Crystal_Ball_function. (visited 25 - 7 2020)
- [33] https://en.wikipedia.org/wiki/Johnson%27s_SU-distribution. (visited 8 - 5 -2022)
- [34] Aaij, R. et al., [LHCb Collaboration], 2020. "Measurement of the $\Lambda_b^0 \rightarrow J/\psi\Lambda$ angular distribution and the Λ_b^0 polarisation in pp collisions." *JHEP06*, 110.
- [35] [LHCb collaboration], 2015. "Measurement of the track reconstruction efficiency at LHCb." JINST, 10 P02007.
- [36] Aaij, R. et al., [LHCb Collaboration], 2019. "Measurement of b hadron fractions in 13 TeV pp collisions." *Phys. Rev. D* 100, 3, 031102.
- [37] Martinez, Santos, D. F. Dupertuis, [NIKHEF] 2014. "Mass distributions marginalized over per-event errors." Nuclear Instruments and Methods in Physics Research Section A: Accelerators, Spectrometers, Detectors and Associated Equipment 764, 150-155.
- [38] <https://root.cern.ch/doc/master/classRooHypatia2.html>.(visited 13-07-2022)